THESIS FOR THE DEGREE OF LICENTIATE OF ENGINEERING

Nanoplasmonic Spectroscopy of Single Nanoparticles

Tracking Size and Shape Effects in Pd Hydride Formation

SVETLANA SYRENOVA

CHALMERS

Department of Applied Physics

CHALMERS UNIVERSITY OF TECHNOLOGY

Gothenburg, Sweden 2014

Nanoplasmonic Spectroscopy of Single Nanoparticles
Tracking Size and Shape Effects in Pd Hydride Formation
SVETLANA SYRENOVA

Department of Applied Physics
Chalmers University of Technology
SE-412 96 Gothenburg
Sweden
Telephone + 46 (0)31-772 3007

Cover:
Left: An illustration of an Au nanodisc dimer with a small Pd particle in the gap (image courtesy of Carl Wadell), accompanied with a top-view (lower left) and a side-view (lower right) SEM images of the nanofabricated structures. Right: An illustration of an Au nanosphere and a Pd nanocube in its vicinity, accompanied with a top-view TEM (upper right) and a side-view SEM (lower right) images of the wet-chemically synthesized nanostructures. Both types of nanostructures are used for investigation of H_2 (red dots) absorption in Pd nanoparticle with Au unit in each case serving as nanoantenna.

Printed at Chalmers Reproservice
Gothenburg, Sweden 2014

Nanoplasmonic Spectroscopy of Single Nanoparticles
Tracking Size and Shape Effects in Pd Hydride Formation

Svetlana Syrenova
Department of Applied Physics
Chalmers University of Technology

Abstract

Localized surface plasmon resonance (LSPR) is a phenomenon of collective oscillation of conduction electrons in metal nanoparticles smaller than the wavelength of light that is used for its excitation. Plasmonic metal nanoparticles are able to confine light to extremely small volumes around them, i.e. below the diffraction limit. This gives rise to strongly localized and enhanced electromagnetic fields in so-called "hot spots" of the plasmonic nanoparticle. These hot spots usually correspond to the edges, sharp corners or tips of monomer structures, and, in case of coupled multimer arrangements, to the antenna junctions. Plasmonic hot spots are highly advantageous for sensing, since any object that is inserted there will influence the optical resonance of the system via coupling to the local field. Placing a well-defined catalytic nanoobject in the hot spot of a plasmonic nanoantenna offers thus unique possibilities to obtain detailed information about the role of specific features (e.g. facets, size, shape or relative abundance of low-coordinated sites, etc.) of that particle for its functionality/activity at the single particle level. Consequently, there is an increasing interest to use plasmonic antennas as a tool to investigate catalytic processes in/on single functional nanomaterials *in situ*. Single particle measurements are possible with the use of dark-field scattering spectroscopy, since plasmonic nanoparticles efficiently scatter light and are easily observable in the dark-field microscope. In this context, this work was dedicated to: 1) Development of a fabrication method for making plasmonic nanoantenna structures with the possibility to place a nanoparticle of interest (catalyst) in the hot spot of the antenna. 2) Investigation of the role of size and shape in hydride formation thermodynamics of wet-chemically synthesized single palladium (Pd) nanocrystals. The latter was possible by attaching the Pd nanocrystal to a plasmonic nanoantenna (gold sphere) by means of electrostatic self-assembly. The role of size was investigated for Pd nanocubes ranging from 20 to 50 nm. The role of shape was considered by modulating the Pd nanocrystal shape from cube to rod and octahedron.

Keywords: localized surface plasmon resonance, plasmonic sensors, palladium nanoparticles and nanocrystals, hole-mask colloidal lithography, shrinking-hole colloidal lithography, metal-hydrogen interactions, single particle spectroscopy, dark field scattering spectroscopy, nanoscale effects, enthalpy of formation

List of appended papers

This thesis is based on the work presented in the following publications:

Paper I

Shrinking-Hole Colloidal Lithography: Self-Aligned Nanofabrication of Complex Plasmonic Nanoantennas

Svetlana Syrenova, Carl Wadell and Christoph Langhammer

Nano Letters **14**, 2655-2663, doi:10.1021/nl500514y (2014)

Paper II

A Versatile Self-Assembly Strategy for the Synthesis of Shape-Selected Colloidal Noble Metal Nanoparticle Heterodimers

Tina A. Gschneidtner, Yuri A. Diaz Fernandez, Svetlana Syrenova, Fredrik Westerlund, Christoph Langhammer, and Kasper Moth-Poulsen

Langmuir **30**, 3041-3050, doi:10.1021/la5002754 (2014).

Paper III

Indirect Plasmonic Nanospectroscopy of the Hydride Formation Thermodynamics in Individual Shape-Selected Pd Nanocrystals with Different Size

Svetlana Syrenova, Tina A. Gschneidtner, Yuri A. Diaz Fernandez, Giammarco Nalin, Dominika Świtlik, Fredrik Westerlund, Tomasz J. Antosiewicz, Kasper Moth-Poulsen and Christoph Langhammer

In manuscript

Related papers not included in this thesis

Nanoplasmonic sensing for nanomaterials science

Elin Larsson, Svetlana Syrenova and Christoph Langhammer

Nanophotonics **1**, 249, doi:10.1515/nanoph-2012-0029 (2012).

Plasmonic hydrogen sensing

Carl Wadell, Svetlana Syrenova and Christoph Langhammer

Invited Review submitted to ACS Nano

My contribution to the appended papers

Paper I: I fabricated the samples, did the experiments and wrote the first draft of the paper.

Paper II: I did part of the experiments and wrote a part of the paper.

Paper III: I did the experiments and wrote the first draft of the paper.

Contents

1 INTRODUCTION

Nanoparticles surround us everywhere – just look at your silver (Ag) spoon (if you happen to have one with an electron microscope at hand): it's producing nanoparticles as we speak[1]! Ancient Romans[2] and Egyptians[3] were among the first to exploit nanoparticles for their needs such as hair dyeing or for colouring vessels. Most likely they did not know what *exactly* they were doing; after all, it was not in an era of rapid development of nanofabrication and characterization techniques. On the contrary, scientists nowadays are able to not only study the nature-made nanoparticles (the ones contained in, for example, sand, dust, volcanic ash, etc. or biological matter like viruses, DNA and biomolecules) or incidentally-man-made nanoparticles ("spoon case" above or other by-products of daily human activities such as soot produced by car engines or simply by burning a candle), but can also engineer nanoparticles of their own! The latter is to a large extent what this thesis is about – to design and create understanding of engineered nanoparticles with well defined sizes, shapes and composition. The simplest reason for the "why" being human's curiosity to reveal the secrets of the (nano)world by carefully exploring its tiny inhabitants. How and why nanoparticles behave as they do? On a larger scale, however, we have seemingly infinite motivations to tame nanoparticles for the benefit of mankind. Nanoparticles can potentially help prevent[4] or even cure diseases[5,6], save the Earth from pollution[7,8] and play an important role in the development of efficient and sustainable energy sources[9].

From this introduction it becomes clear that there is an immense variety of questions one can ask and study about nanoparticles, and thus it is hard to embrace them all. Therefore, this work is mainly focused on studying the interaction of a nanoparticle with its surrounding environment. Among these interactions the focus is placed on events such as adsorption or desorption of species on/from the particle, as such processes, for example, are centrally important steps in every catalytic reaction. The following paragraphs thus introduce the concept of catalysis, techniques for how to study catalyst nanoparticles and challenges in this direction.

1.1 What is a catalyst?

First of all, what is a catalyst? If there was a (re)action movie to be made, starring chemical A and chemical B that together form product P, a catalyst could play a guy that comes in with a line: "We can do this the hard way or the easy way". In other words, a catalyst is a substance that facilitates a chemical reaction by lowering the

activation energy that is needed for the reaction to occur. In a catalysed process, reactants A and B spontaneously adsorb to the catalyst, maybe dissociate, and react with each other while they are bound to it. The activation energy of the rate limiting elemental reaction step along this reaction pathway is significantly lower than that in the corresponding uncatalysed reaction. Typically, for A and B reacting in gas or liquid phase, catalysed reactions are also thermodynamically downhill, i.e. they are exothermic and lead to a decrease in the free energy. This way, a catalyst is able to significantly enhance the rate of reaction or change the distribution of the reaction products selectively towards specific compounds. When the product is formed, it detaches from the catalyst and leaves it unaltered and unconsumed during the process, so that the catalyst is available for the next reaction event. While the overall change in free energy is the same both for catalysed and uncatalysed reactions, the kinetic barriers are lowered.

There are three types of catalysts: biocatalysts (enzymes and cells), homogeneous catalysts and heterogeneous catalysts. In heterogeneous catalysis, as opposed to the homogeneous, the catalyst and reactants are in different states, i.e. solid, liquid or gas. In the majority of cases, the catalyst material is a solid, and reactants are molecules in the gas or liquid phase. Heterogeneous catalysts can be metals, oxides, sulfides, carbides, nitrides – practically any type of material – supported (nanoparticles) or bulk. The support can be either amorphous (e.g. porous alumina, silica, carbon (C)) or crystalline (zeolites), and mainly serves as a template with high surface area and porosity that allows maximizing the total number of active sites per unit volume of the catalyst. Supported nanoparticle catalysts are especially interesting (and constitute the majority of industrial catalysts) since they provide large surface area per unit mass, and therefore such nanocatalysts are more effective. In addition, the smaller the particle the larger abundance of undercoordinated sites such as edges and corners that are usually characterized with high reactivity.

1.2 Why study catalysts?

Catalysts are very important in the chemical industry, for energy production and pollution mitigation. This is due to the fact that uncatalysed reactions can be several orders of magnitude slower and much more “expensive” than their counterparts due to amount of energy that is required for the reaction to occur. Moreover, sometimes, it is simply not feasible to achieve a certain product without a catalyst because of high activation barriers. Thus, the vast majority of existing chemical products and fuels involve catalytic processes at some point during their production. Therefore, the need for understanding, and to either optimize existing catalysts or design new ones, is tremendous both from an economical and environmental point of view.

A perfect catalyst is active, selective and durable, but reality is that the catalysts are not always perfect. Moreover, the catalyst has to facilitate the reaction at an appropriate rate and under acceptable temperature and pressure conditions in order to be efficient. Lowering the catalyst’s working temperature and pressure, as well as the

amount of reaction by-products, is a goal largely sought after. If achieved, it can decrease the production costs, energy consumption, the amount of "waste" produced during a catalytic process, and the amount of material that is consumed by the reaction. The latter is significant since industrial catalysts in many cases can involve expensive and scarce materials such as Pd (palladium), platinum (Pt) or rhodium (Rh). Therefore designing new more efficient and/or cheap(er) catalysts is highly relevant. In order to reach these incentives it is important to understand how the catalyst works: what are the active sites (not all the atoms/regions of the catalyst are involved in a real catalytic process), their structure and properties, and how they interact with all the reaction participants (reactants, intermediates and products). In addition, for nanoparticle catalysts a lot of research effort is put into understanding what are the optimal size, composition, shape, and surface structure of the nanoparticle to achieve the goal of catalysis by design.[10]

1.3 Challenges in catalyst characterization

Catalysts and catalytic processes are very complicated systems: a catalytic reaction can involve multiple steps and is highly dependent on the surrounding environment (temperature, pressure, reactants), the structure and chemistry of the support material and the catalyst itself. Studying a catalyst is thus a real challenge: the scientist is always facing a dilemma of how much information about the catalyst one can obtain with a certain technique and how relevant this information can be with respect to a real catalytic process. For example, to simplify the investigation of the catalyst one can use well-defined model systems such as supported nanoparticles (e.g. fabricated arrays of nanoparticles) or single crystals, and study them under well-defined ultrahigh vacuum (UHV) conditions. With the help of powerful surface science techniques this approach has given a lot of valuable insight into catalytic processes, especially for fundamental science. However, there are two major problems with such an approach: 1) a catalytic reaction proceeds very differently under UHV conditions compared to the real reaction conditions that involve high pressures; this is referred to as the *"pressure gap"*. And 2) the reactivity is very different for a simplified structure compared to an industrial "real" catalyst; this is referred to as the *"material"* or *"structure gap"*. Consequently, it is not straightforward to relate information obtained in idealized experiments to the catalytic processes happening under realistic reaction conditions in chemical industry. Therefore, the development of characterization techniques to investigate catalysts and catalytic processes *in situ* (while the reaction is happening) is very relevant and, at the same time, a challenging task. *In situ* studies enable identification and understanding of important steps such as formation of reaction intermediates and nature of the active sites, as well as of the important stages in catalyst lifetime, e.g. activation/deactivation. Requirements applicable to the ideal *in situ* technique for studies of catalytic processes are highly demanding: it should be very sensitive, have very high spatial (below nanometers) and temporal (down to milliseconds and ideally even less) resolution and allow monitoring simultaneously both properties of the active site (structure, composition, activity) and the reaction

intermediates. At present, there is no existing technique that meets all of the above requirements, and instead it is necessary to combine several different approaches in order to get a more complete picture. A variety of techniques today allow investigation of either *morphological properties of the catalyst* (e.g. electron probes (scanning electron microscopy (SEM), transmission electron microscopy (TEM)) and scanning probes ((atomic force microscopy (AFM), scanning tunneling microscopy (STM), X-rays (X-ray diffraction (XRD))) or *surface chemistry associated with catalytic process and reaction mechanism* (infrared spectroscopy (IRS), Raman spectroscopy, neutron scattering (NS), X-ray absorption spectroscopy (XAS) and deviations like Extended X-ray Absorption Fine Structure (EXAFS) or X-ray Absorption Near-Edge Structure (XANES), electron paramagnetic resonance (EPR), ultraviolet-visible spectroscopy (UV-vis), etc.). The tradeoff between these techniques is that the ones, which offer spatial resolution to resolve morphological properties of a catalyst down to nm scale, do not have sufficient temporal resolution for studies of the fast catalytic events and kinetics of the processes. Therefore, it is also useful to employ theoretical studies and modeling (e.g. density functional theory (DFT), Monte Carlo (MC) simulations, molecular dynamics (MD)), to conceptually understand and/or predict the properties of the catalyst and the reaction steps.[11]

Another difficulty in exploring nanocatalysts is that traditional studies aim at the ensembles of nanoparticles that can be very inhomogeneous in terms of size, shape and structure of the individual catalyst nanoparticles. Keeping in mind the sheer complexity of a heterogeneous catalyst, such ensemble-averaged measurements may mask details and the true mechanism of the processes involved, i.e. how these relate to details in catalyst nanoparticle size, shape and composition. This may complicate identification of advantageous structural and/or compositional properties that an optimal catalyst should have. Therefore, single particle studies of catalytic reactions performed *in situ* and in real time are of crucial importance in catalysis development.

1.4 Techniques for single catalyst nanoparticle characterization

In the last decade, several experimental approaches have become available that allow monitoring catalytic events on a single nanoparticle. These techniques include electrochemical methods (e.g. electrochemical scanning probe microscopy[12], electrochemical measurements with ultramicroelectrode[13] or electrocatalytic current amplification via single-nanoparticle collisions[14]), single-molecule fluorescence microscopy[15] and surface-enhanced Raman spectroscopy[16]. These methods detect the amount of reactants consumed or products generated in a catalytic reaction by a single nanoparticle. The detection scheme is based on the fact that reactants and products in a catalytic reaction can affect, for example, the current in electrochemical measurements (proportional to the rate of reactant consumption or product generation); in case of fluorogenic reactions, reactants can be transformed into a fluorescent product; or

reactants can have distinct vibrational features suitable for detection with Raman spectroscopy.

Other methods, instead, focus on the changes of the catalyst particle itself in their detection scheme. For example, alterations in the oxidation state or coordination environment of the atoms can be monitored by X-ray microscopy[17]. Chemical or physical properties of a catalyst and its surroundings can change due to consumption of reactant molecules and product generation on the catalyst surface. This can be monitored by surface plasmon resonance spectroscopy, which is based on the phenomenon of LSPR. Briefly, LSPR is a coherent oscillation of conduction electrons in metal nanoparticles. The LSPR frequency of such a particle depends on its size, shape, material and surrounding environment. For nanoparticles of Au and Ag, which are common plasmonic materials due to their favourable optical properties, the LSPR wavelength is in the ultraviolet-visible-near-infrared (UV-vis-NIR) regime. In this regime, the scattering spectra of individual plasmonic nanoparticle can be measured with dark-field scattering spectroscopy. In general terms, the LSPR sensing approach is to detect changes in LSPR frequency (e.g. wavelength shifts) of the sensor particle caused by the alterations of the sensor particle itself or in the surrounding environment of the sensor (direct[18] and indirect[19] sensing). In this thesis, nanoplasmonic sensing was the main characterization tool used and further developed, and therefore it is discussed in more detail in Chapter 2, which gives a basic introduction to the phenomenon of LSPR. [20,21]

Another important technique for single nanocatalyst characterization that should be mentioned here is environmental TEM (ETEM), which is capable of *in situ* studies of chemical processes at gas–solid interface with atomic scale resolution.[22-24] It should be noted however, that most of the time, the information obtained with ETEM is at gas pressures of few millibars, and not at ambient pressure, which is more relevant for technological applications. Nevertheless, there are possibilities to bridge the pressure gap in ETEM by utilizing nanoreactors that allow atomic-resolution ETEM at ambient pressure and elevated temperature conditions[25].

1.5 The scope of this thesis

This thesis is an attempt to develop a non-invasive experimental method for probing single nanoparticles in a catalytic reaction under ambient conditions (i.e. various temperatures, atmospheric pressure) using nanoplasmonic sensing. For the purpose of this thesis, two routes were explored: 1) optimization of plasmonic sensing structure via surface-based nanofabrication of plasmonic nanoantennas with high sensitivity in order to be able to probe catalytic events, and 2) the possibility to probe a nanocatalyst with well-defined sizes and shapes, which were achieved via wet-chemical synthesis of nanocrystals.

In the first part of this work, a nanofabrication method was developed for making plasmonic nanoantenna structures, such as nanodisc dimers and trimers, which are characterized by high field enhancement (advantageous for sensing) in so-called *hot*

spots of the antenna (i.e. narrow gaps in the dimer/trimer arrangements). As the key result, the targeted ability of the fabrication scheme to allow placement of a catalyst particle of interest (nanocatalyst) in the plasmonic hot spot was realized.

In the second part of this work, the possibility to probe wet-chemically synthesized single Pd nanocatalyst particles of various sizes (15-70 nm) and shapes (i.e. cubes, dodecahedra, rods, octahedra) was explored. This was made possible by linking the plasmonic antenna nanoparticle to the catalyst particle by means of electrostatic self-assembly in solution with subsequent deposition of the assembled dimers onto a surface. These nanoparticle arrangements were then characterized with SEM, before their behavior upon exposure to hydrogen and during hydride formation was investigated as a function of their size and shape (see Chapter 3 for more details). Hydrogen absorption in/on Pd was chosen as the (model) reaction for this work due to several reasons. First, it should be noted that the hydrogen storage in Pd is not a "true" catalytic process, however, it is a first step towards the long-term goal that motivates this work, i.e. exploration of "real" catalytic processes. From experimental point of view, hydrogen absorption in Pd occurs at "convenient" conditions, i.e. around room temperature and at pressures below 1 bar. In addition, the hydride formation in Pd is completely reversible, and the kinetics of the process are reasonably fast even at room temperature, since there are no or very low kinetic barriers for hydrogen (H_2) sorption and diffusion in Pd. Finally, even though the bulk Pd-hydrogen system is very well studied, there are still open questions about the physics of hydride absorption in nanoscale Pd systems. Specifically, detailed studies of the role of Pd nanoparticle size and shape on the thermodynamics and kinetics of the hydride formation process have started to emerge only very recently and require further attention[26,27]. For example, since most of the work so far has been done on ensembles of Pd nanoparticles, it is still unclear if some of the observed effects stem from the intrinsic size/shape properties or due to inherent inhomogeneity of the ensemble particles. One such example is the characteristic slope of the two-phase coexistence plateau that emerges upon nanosizing of the Pd. Single particle studies are therefore crucial in resolving such issues. At a more general level, deeper understanding of the physics behind these nanoscale size and shape effects can facilitate the development of more efficient hydrogen storage systems and catalyst materials.

2 NANOPLASMONICS

When light interacts with metal particles with a size, *a,* smaller than the wavelength of light, λ, it invokes resonant collective oscillations of free electrons in the particle - the localized surface plasmon resonance (LSPR). This happens since light can penetrate the whole particle due to its small size and thus "grasp" all of its conduction electrons. LSPR is established when the frequency of the incoming light wave matches the resonance frequency of the electrons oscillating against the restoring force of the positive atomic cores of the metal particle. This electron cloud displacement causes the formation of a dynamic dipole (Figure 1), which leads to the enhancement of the electromagnetic field around the particle with respect to the incoming field and constitutes a spatially confined *sensing volume* around the particle[28]. The LSPR frequency is known to be dependent on particle parameters such as size, shape and material, as well as on the dielectric properties of the surrounding environment of the particle. By monitoring the LSPR wavelength of the plasmonic particle it is thus possible to detect changes of the particle itself and of its surroundings, which is the basis of plasmonic sensing. At the LSPR frequency the particle efficiently absorbs and scatters light. In the next paragraph these terms are briefly described with regard to the metal nanoparticle. This is followed by a short discussion of the role of particle size, shape and material in nanoplasmonics.

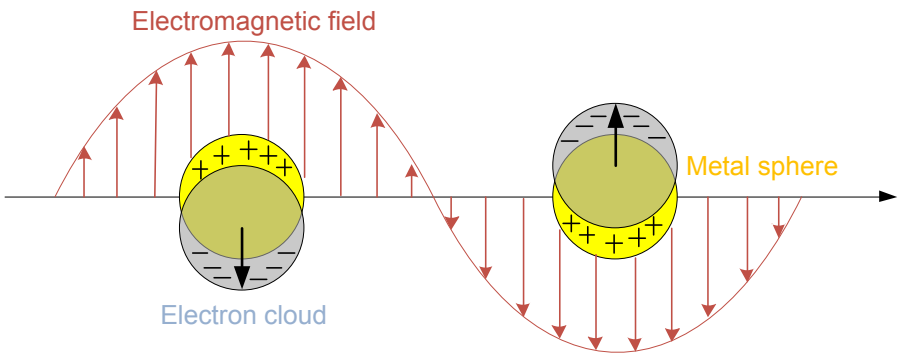

Figure 1. *Schematic representation of a metal nanosphere during LSPR excitation by an external alternating electromagnetic field at two different times.*

2.1 Extinction, scattering and absorption of light in metal nanoparticles

Propagation of light through a disperse medium can be described in terms of two mechanisms: *absorption*, when light is absorbed into the matter, and *scattering*, when light is forced to deviate from a straight trajectory due to the non-uniformity of the medium. These mechanisms can be expressed through respective cross-sections that are defined as the effective area, which governs the probability of either a scattering or an absorption event. The total sum of these two gives rise to the so-called *extinction* cross-section that describes the area of total flux scattered and absorbed by the object.

Spherical particles are simple structures that support plasmon resonances. German physicist Gustav Mie in 1908 presented[29] an exact solution of Maxwell's equations for an incoming plane wave interacting with a spherical particle of arbitrary size and composition, using which, one can obtain expressions for the extinction and scattering cross-sections of such a particle. When the particle is smaller than the wavelength of light, i.e. $a<<\lambda$, one can make the so-called quasistatic approximation for solving Maxwell's equations. It makes the assumption that so-called retardation effects can be ignored, which means that variations of the phase of the external field across the particle can be assumed negligible, so that the incident plane wave can be approximated by a constant field. The quasistatic approximation thus allows simplifying the full Mie expansion of Maxwell's equations. Such a basic model is useful for understanding how the material in and around the particle influences the LSPR. For a spherical nanoparticle in the quasi-static limit, the aforementioned cross-sections can be described by the following expressions:[30]

$$\sigma_{sca} = \frac{8\pi}{3} k^4 \cdot a^6 \left(\frac{\varepsilon_m - \varepsilon_d}{\varepsilon_m + 2\varepsilon_d}\right)^2 \tag{2.1}$$

$$\sigma_{ext} = 4\pi k a^3 \cdot Im\left(\frac{\varepsilon_m - \varepsilon_d}{\varepsilon_m + 2\varepsilon_d}\right) \tag{2.2}$$

$$\sigma_{abs} = \sigma_{ext} - \sigma_{sca} \tag{2.3}$$

where k is the wave number ($k=2\pi/\lambda$), a is the radius of the particle, ε_d is the dielectric function of the surrounding medium, and ε_m is the dielectric function of the metallic nanoparticle. As can be seen from Eq. 2.1-2.3, extinction scales as the particle volume (a^3) and scattering scales as the particle volume squared (a^6). It is also apparent that the scattering and absorption of the particle are influenced by the dielectric functions of both the particle itself and its surrounding medium. As follows from Eq. 2.1-2.3, the maximum in scattering and extinction cross-sections should happen at the condition:

$$\varepsilon_m + 2\varepsilon_d = 0 \tag{2.4}$$

which is the resonance condition for the LSPR.

If now one considers a dielectric function of a metal as predicted by the Drude model (which, in brief, uses the simplest approximation to describe the optical properties of metals by assuming that all conduction electrons are "free" like atoms in a gas):

$$\varepsilon_m = 1 - \frac{\omega_p^2}{\omega^2 + i\gamma\omega} \tag{2.5}$$

where ω_p is the plasma frequency of a metal, i.e. the frequency below which the reflectivity of any metal is equal to unity for frequencies of the external perturbation. Then combining the last two equations (Eq. 2.4 and 2.5) gives an expression for the LSPR frequency:

$$\omega_{max} = \frac{\omega_p}{\sqrt{2\varepsilon_d + 1}} \tag{2.6}$$

Eq. 2.6 can be re-written in terms of the wavelength:

$$\lambda_{max} = \lambda_p\sqrt{2\varepsilon_d + 1} \tag{2.7}$$

where λ_p is the wavelength corresponding to the bulk plasma frequency of the metal. From the latter expression it is clear that the wavelength position of the LSPR will depend on dielectric function of the particle surroundings, as well as on changes of the plasma frequency (or, in other words, electron density) of the particle. This is the fundamental effect exploited by nanoplasmonic sensing.

2.2 Dependence of LSPR on shape, size and material of the nanoparticle

2.2.1 Shape

The scattering, absorption and extinction cross-sections of particles that have high spherical symmetry like spheres and ellipsoids can be calculated with high precision using Mie theory. However, different particle shapes other than a sphere can be efficiently used to further tune the LSPR over a wide wavelength range. Nowadays, with advances of nanotechnology, it is possible to prepare nanoparticles of a variety of different shapes and sizes and their optical properties have to be calculated using different theoretical tools. Theoretical modeling of nanoparticles with arbitrary shapes and sizes provides better understanding and improvement of current LSPR sensing schemes (as well as other incentives of nanophotonics). There are several techniques available that allow calculation of different particle shapes and sizes, among which we find: discrete dipole approximation (DDA), finite difference time domain (FDTD) method, T-matrix method, the multiple multipole method, and the modified long

wavelength approximation (MLWA). Utilization of different calculation schemes yields different predictions for the nanostructure resonance. [31,32]

The DDA method has been basis of many papers that analyze various particle shapes and their advantages for LSPR sensing. For example, Jain *et al.*[33] calculated optical properties of Au nanoparticles in the form of nanospheres, nanorods and nanoshells for the purpose of applications in biological imaging and biomedicine. In another paper by Hao *et al.*[34] the shape effect in Ag nanoparticles is considered on examples of a triangular prism, a rod and an oblate spheroid. Other simulation approaches mentioned above have been utilized for studying nanostars[35], nanorice[36], nanoeggs[37] and nanocups[38], to name a few.

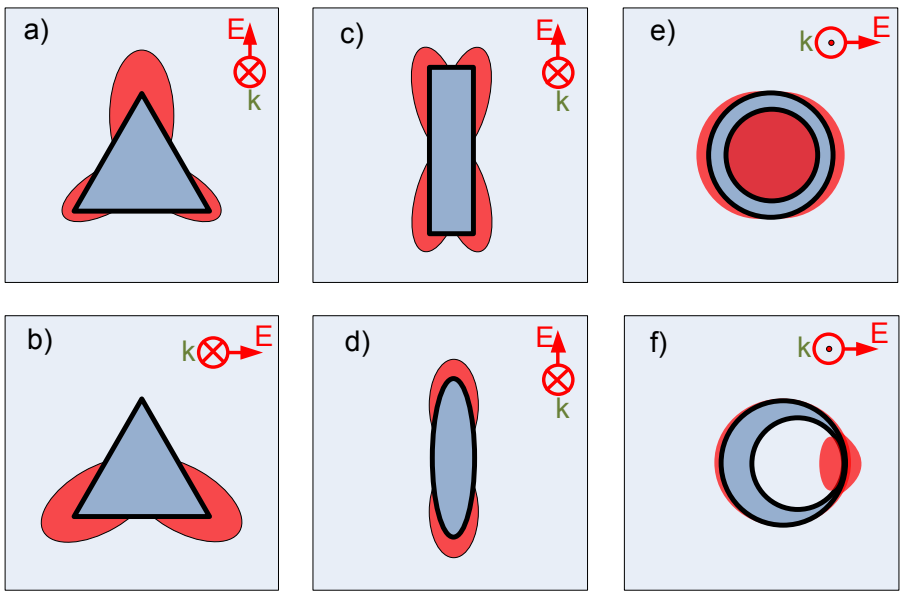

Figure 2. *Schematic representation of plasmonic hot spots for different nanoparticle shapes in terms of electric field enhancement: (a) and (b) triangular prism with polarisation of the exciting field along two different symmetry axes; (c) and (d) rod and prolate spheroid with polarisation of the exciting field along their long axes; (e) nanoshell and nanoegg. Pictures are redrawn from Hao et al.*[34] *and Wu et al.*[37]

One important conclusion from such studies in the quest of ideal particle shape for LSPR sensing is that there exist so-called hot spots in plasmonic nanostructures. These hot spots are the regions on the nanostructure surface or in its vicinity, where there is the largest (for each individual shape) enhancement of the electromagnetic field. Generally, strong field focusing behavior is observed at the sharp edges or tips of the nanostructures, and field enhancement tends to increase with prolate shapes. In addition, when the particle has irregular shape (other than sphere), in order to obtain the highest enhancement of the electromagnetic field, it becomes important to excite

LSPR with the appropriate polarization of light. Figure 2 schematically shows the polarization-dependent electromagnetic field enhancement around different nanostructures. Note that the magnitude of this enhancement can be very different for each case, because it strongly depends on the size and material of the nanostructure, and its distribution is only depicted schematically. Figure 2 thus only serves to illustrate the notion of the concept of a plasmonic hot spot.

2.2.2 Size

If the condition $a \ll \lambda$ is no longer valid (i.e. the particle is comparable to the wavelength of light), retardation effects arise: 1) the field outside the whole particle becomes inhomogeneous; 2) it takes finite time for the plasmonic dipole field to travel through the particle and thus it is not homogenous inside. As a consequence, there is a phase shift between exciting field and dipolar field. In addition, due to field inhomogeneity and since any external field can be expanded in multipoles, the plasmon excitation can have higher order modes other than dipolar ones (i.e. quadrupolar, octopolar, etc.), and as the particle size increases these modes become more significant (as well as with asymmetric particle shapes).

Another effect caused by increasing particle size is an increase of radiation damping that is caused by energy loss of the radiating dipole via photon emission (light scattering) in the particle[39]. The size of the nanoparticle is proportional to the square of the dipole moment, which in turn is proportional to the dipole radiative strength, thus the radiative plasmon decay channel starts dominating with increasing particle size. All these effects accompanying an increase in particle size typically result in a shift of the LSPR, and thus of the corresponding spectra, to longer wavelengths, and in spectral broadening of the LSPR peak.

In the case of small spherical particles, as follows from Eq. 2.6, the size doesn't play a role in determining the spectral position of LSPR, since there is no geometric factor involved (however, this is not completely true for very small particles (<10 nm), where the dielectric function of the metal becomes size dependent and surface scattering effects may become appreciable). The volume only determines the magnitude of the scattering and absorption cross-sections. As can be seen from Eq. 2.1-2.3, the scattering has a square dependence on the volume, while extinction is only linearly volume-dependent. Therefore, as the particle gets smaller, it is harder to see scattered light from it because with decreasing particle size more and more light gets absorbed.[40]

2.2.3 Material

Traditional plasmonic materials are the noble metals Au and Ag. This is due to the fact that they have strong and spectrally relatively narrow plasmon resonances at optical frequencies. This can be partly explained by the high electron density of these metals: the more electrons involved in a plasmon oscillation, the higher is the resonance

frequency. Another reason is that, at visible frequencies, the losses in Au and Ag are relatively low compared to other metals (e.g. copper (Cu), Pd, Pt).

The features such as electron density and intrinsic losses are determined by the electronic band structure of the material, which describes the range of energy (i.e. energy bands) that an electron can have within a solid. At zero temperature all low energy states up to a certain energy level, i.e. the Fermi energy, will be filled with electrons, and the states above this level will be empty. In contrast to Au and Ag, where the energy bands with the highest density of states (d-bands) are located below the Fermi energy, metals like Pd and Pt have their d-bands situated such that they cross the Fermi level. This increases the possibility for interband excitations over the whole UV-vis-NIR spectrum range. The latter leads to stronger damping of plasmon resonance via interband electron-hole pair formation (i.e. absorption)[41]. This is the main reason for the strong damping and low scattering (radiative decay) observed for LSPR in Pd and Pt nanoparticles, even for large particle sizes. More on band theory can be found in literature by authors such as e.g. Kittel[42]. In summary, Ag is the best material in terms of the "quality" of its LSPR owing to its intrinsically low losses. Au is not quite as efficient but at the same time more chemically inert and therefore more favourable for applications. This is illustrated in Figure 3, which shows what happens with an unprotected Ag nanoparticle after few weeks in air.

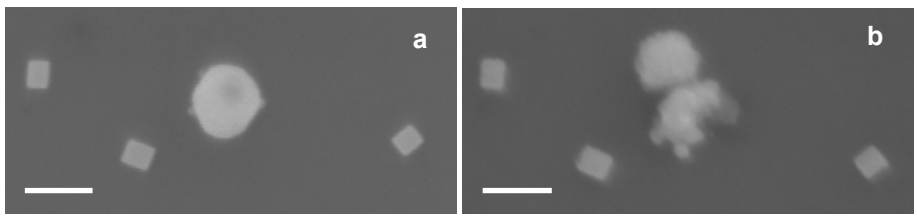

Figure 3. *The SEM images of the synthesized Ag nanosphere with three Pd nanocubes around it: (a) as synthesized and deposited on the substrate; (b) after 3 weeks that the sample spent in the storage box. After some time in air the Ag particle becomes oxidized and its appearance drastically changes. The scale bar in the SEM images is 100 nm.*

Finally, it is also worth mentioning that not only metals can support LSPR but (at infrared frequencies) also metal oxides (e.g. indium tin oxide)[43], and semiconductors (e.g. copper sulfide[44], copper selenide[45]) with appreciable free electron densities, as well as graphene.[46,47] Semiconductors are especially interesting for nanoplasmonics since their free electron concentrations can be tuned by doping, temperature and/or phase transitions. For example, heavily hydrogen doped semiconductors such as zinc oxide and titania (TiO_2) are proposed[48] for creating highly efficient noble-metal-free plasmonic photocatalyst systems. As for graphene, it has already been shown to possess unique mechanical, electric, magnetic and thermal properties,[49] and in addition it also has remarkable optical properties.[50] Graphene can support surface plasmons,

and furthermore its optical properties can be modified by gating, by doping, by chemical means and through functionalization with conventional noble metals.

2.3 LSPR in dimers

Up to date, a large number of theoretical and experimental studies[34,51-59] have established the knowledge that there is strong coupling between two plasmonic nanostructures if they are placed in close vicinity. Qualitative interpretation of this phenomenon can be given based on the simple dipole-dipole interaction model.[52] The electromagnetic field applied to a single plasmonic nanoparticle creates surface charges that feel a repulsive force (Figure 4a). This matches the resonance condition of the plasmonic excitation. However, when there are two nanoparticles in close proximity to each other, depending on polarization, additional forces act on the particle pair, as sketched in Figure 4. If the polarization of the electric field is parallel to the long axis of the particle pair, the positive charge of the left particle faces the corresponding negative charge of the right particle (Figure 4b). Such charge distribution of two adjacent particles creates attractive forces between them, whereas the repulsive forces within each particle become weaker. This leads to a lower resonance frequency of the coupled system. Contrary, in case of perpendicular electric field polarization, the charge distribution of two particles cooperatively enhances the repulsive force between them (Figure 4c), which leads to an increase in resonance frequency.

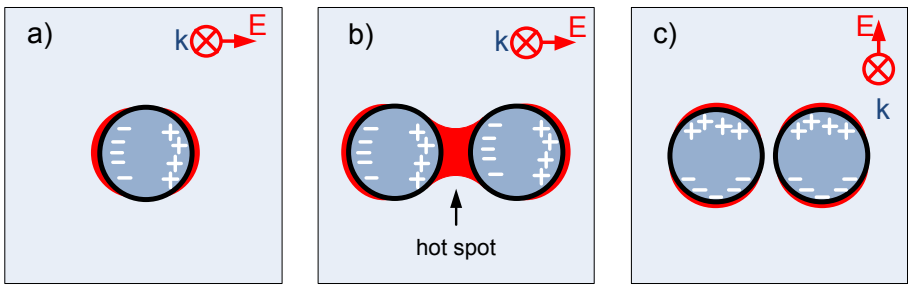

Figure 4. *Schematic illustration of electromagnetic interaction in (a) an isolated particle, (b) a pair of particles with electric field polarization parallel to their long axis and (c) perpendicular to their long axis (no strong hot spot in the dimer occurs). Pictures are redrawn from Rechberger et al.*[52]

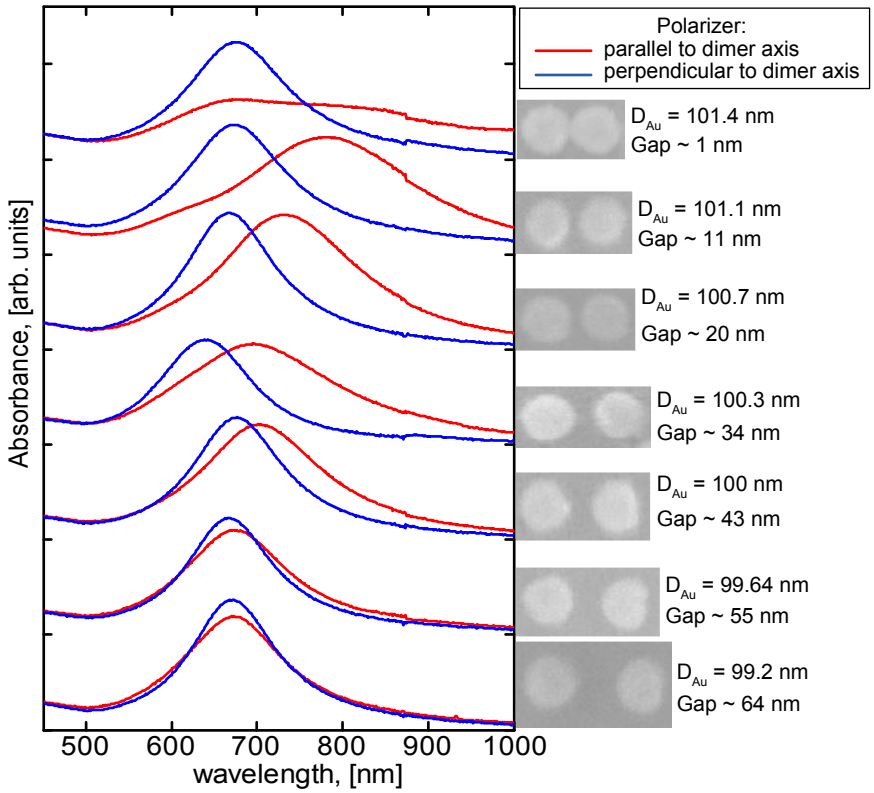

Figure 5. *Polarization dependent absorbance spectra of Au nanodisc dimers prepared on glass substrate by HCL, and corresponding environmental SEM images. As the dimer gap increases, the difference in excitation of light with parallel and perpendicular polarization along the dimer axis becomes negligible.*

The strongest field enhancement in the coupled particle (dimer) system occurs in the gap between the particles, the so-called *hot spot.* This small area of intense local field is advantageous for LSPR sensing, since it provides strong coupling to anything trapped in the gap, and which will influence the resonance of the coupled system. The magnitude of the field enhancement in the gap of a dimer can be several times higher than the one in/around a single plasmonic particle.[34,60,61] For example, the square of electric field between two closely spaced spheres or triangles is theoretically estimated to be at least a factor of 10 larger than that around respective monomers[34]. The field enhancement in the gap is a strong function of the gap distance (as illustrated in Figure 5, where absorbance spectra of nanodisc dimers were measured using different polarizations of light), and it scales with particle size, i.e. larger particles can give the same enhancements for larger gap sizes. It has also been shown that the plasmon wavelength shift decays nearly exponentially with increasing inter-particle gap, and

that the decay length is universally independent of the nanoparticle size, shape, the metal type, or the surrounding medium.[62,63] As for the absolute field enhancement in the dimer gap, as well as absolute plasmon coupling strength, similar to the case of isolated particles, they will depend on the shape, size and material of dimer particles. Several particle pair geometries (other than pairs of nanospheres) have been calculated theoretically: pairs of ellipsoidal nanoparticles (spheroids, rods and cylinders)[55] and triangular prisms facing each other tip-to-tip and tip-to-side[34]; or studied experimentally (e.g. pairs of nanoshells[64]). Nevertheless, often the choice of the dimer particle shape is determined by the availability of a suitable fabrication method.

2.4 Single nanoparticle plasmonics

There are several experimental approaches that allow excitation of LSPR in single nanoparticles, and at the same time are capable of probing such an event. These approaches can be divided as far-field (particle is observed from much larger distance than the wavelength of light) and near-field (particle is probed in almost direct proximity to it by a sharp tip or electron beam). The probed phenomenon in the first approach can constitute *scattering* (dark field microscopy), *absorption* (photothermal imaging[65] (PHI)) and *extinction* (spatial modulation spectroscopy[66] (SMS)) of the particle or *electromagnetic field enhancement* around it (surface-enhanced spectroscopy, e.g. surface-enhanced Raman spectroscopy[67] (SERS) or second harmonic generation[68] (SHG) spectroscopy). Consequently, with the second approach, the probed phenomenon would be *near-field optical transmission* or *scattering* (scanning near field optical microscope[69] (SNOM)), *photon-induced field-enhanced electron emission* (photoelectron emission microscopy[70] (PEEM), scanning photoionization microscopy[71] (SPIM)), *electron-induced field-enhanced photon emission* (cathodoluminescence[72]) or *energy loss in a transmitted electron beam due to plasmon excitation* (electron energy loss spectroscopy[73] (EELS)).[74]

Far-field approaches are intrinsically diffraction-limited, however their simplicity and robustness still allow investigating distinguished features of plasmonic nanoparticles such as scattering or absorption. Light scattering by the plasmon particle can be very useful in single particle studies for investigation of materials that have poor scattering properties themselves due to their electronic structure (e.g. catalytic materials such as Pd or Pt as discussed above) or due to their small size, which also lowers scattering efficiency. This is since the intensity of light scattered by a particle is proportional to the square of the particle volume. These limitations can be overcome by employing the plasmonic particle as an indirect probe by placing it in close proximity to the particle of interest, which itself has weak scattering properties. In this way the plasmonic particle can serve as antenna unit that is sensitive to whatever is happening in its surrounding environment (i.e. sensing volume)[75,76] (Figure 6). Therefore, the problem of low scattering efficiency of the particle of interest is eliminated. In this thesis dark field scattering spectroscopy was used as one of the main characterization techniques and is described in detail in Chapter 6.

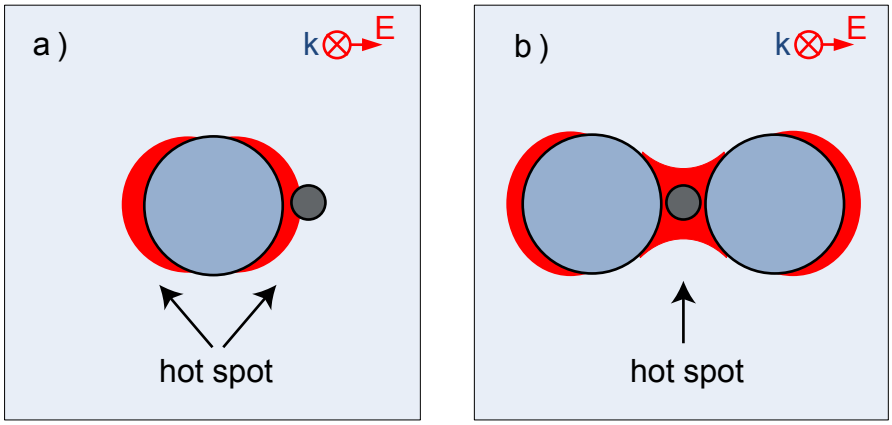

Figure 6. *Illustration of the sensing volume of a plasmonic sphere (a) and a pair of spheres (b). By placing a particle of interest (grey) in the hot spot of the plasmonic antenna it is possible to probe the events in/on the particle with the help of the enhanced electromagnetic fields around the antenna.*

3 METAL-HYDROGEN INTERACTIONS

In this thesis, the fascinating ability of Pd to absorb large amounts of atomic hydrogen is used as a model reaction system. Specifically, Pd nanoparticles are utilized to study the sensing properties of different plasmonic nanoantenna structures, and they are subject of investigation whether their size and shape influence the thermodynamic and kinetic properties of hydride formation. This chapter is dedicated to the discussion of some details in metal-hydrogen interactions that are necessary for understanding this work.

When a metal is exposed to hydrogen atmosphere, the hydrogen molecules may adsorb onto the metal surface and dissociate into atoms. On many metals this is an activated process that does not occur spontaneously at ambient conditions, however Pd demonstrates a high (non-activated) catalytic activity for hydrogen adsorption and dissociation on its surface. After dissociation, the hydrogen atoms start to diffuse into the metal lattice. At low hydrogen gas pressures a solid solution of hydrogen in the host lattice (called the α-phase) is formed. In the α-phase, since the amount of hydrogen is rather low and thus the distance between hydrogen atoms is large, (attractive) hydrogen-hydrogen interactions inside the lattice are very weak. Nevertheless, as the metal absorbs more and more hydrogen, it will locally strain the lattice of the host. As the hydrogen pressure/concentration is increased further, the amount of hydrogen in the metal will increase and eventually hydrogen-hydrogen interactions (resulting from the lattice strain as well as electronic interactions) become appreciable, and the formation of regions of the hydride (β-phase) starts. At this stage the α-phase and β-phase coexist in equilibrium and an incremental increase in the hydrogen concentration around the metal will only result in the growth of the β-phase regions at the expense of the α-phase. Eventually, with continued increase in external hydrogen pressure, the entire metal will be transformed into the β-phase, where the hydride formation is complete, and any further increase in hydrogen pressure will only result in minor changes in the hydrogen content in the hydride. [77]

A common way to study such hydrogen sorption processes is to map (at constant temperature) the hydrogen content in the metal versus the increasing applied hydrogen pressure; thus, a so-called pressure-composition isotherm is obtained (Figure 7a). The isotherm exhibits a clear “plateau” at the pressure where the α- and β-phase coexist, i.e. at the hydride formation pressure. As the temperature is increased, the pressure at which the hydride formation takes place also increases. In this way, by measuring isotherms at several temperatures, the phase diagram of the metal-hydrogen system can be mapped out (the phase boundaries are located on the low and high

concentration sides of the equilibrium plateau, respectively, up to the critical point). From such isotherm measurements, one can obtain useful information about the process, such as change in enthalpy (ΔH) and entropy (ΔS) during the hydride formation/decomposition. The temperature (T) dependence of the plateau pressure is described by the Van't Hoff equation[78]:

$$ln\left(\frac{P}{P_0}\right) = \frac{-\Delta H}{RT} + \frac{\Delta S}{R} \tag{3.1}$$

where P is the plateau pressure, P_0 is the atmospheric pressure and R is the gas constant. ΔH and ΔS can be found by constructing a Van't Hoff plot (Figure 7b), i.e. plotting $ln(P/P_0)$ versus $1/T$, which yields a straight line. Then, ΔH corresponds to the slope, and ΔS to the intersection with the pressure axis, respectively.

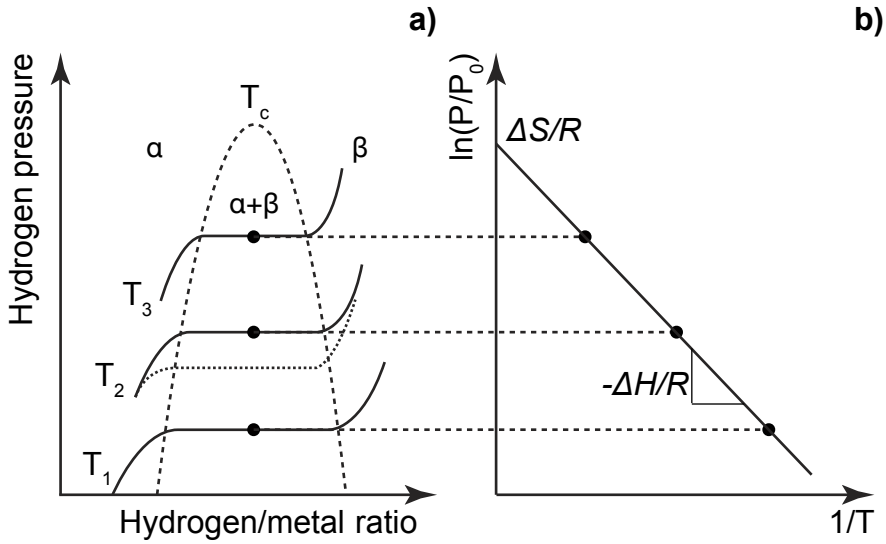

Figure 7. *(a) Sketch of a typical pressure-composition isotherm measured at different temperatures, which allows mapping the phase diagram of the hydride formation/decomposition. The hydride formation is reversible, however the plateau pressure of hydride decomposition often occurs at lower pressure resulting in hysteresis. (b) Van't Hoff analysis, where the equilibrium plateau pressures are plotted against the inverse temperature. The Van't Hoff plot allows obtaining information about the ΔH (proportional to the slope of the straight line) and ΔS (proportional to the intersect with the pressure axis) of hydride formation/decomposition.*

If one reverses the process and decreases the hydrogen pressure around the hydride, the decomposition process will take place in a similar way to the formation described

above, and exhibit a plateau where β-phase and α-phase are in thermodynamic equilibrium as the hydride is decomposed. However, the hydride decomposition will in most cases not occur at the same pressure as the formation, but rather at a lower pressure. This hysteresis (Figure 7a) is also the result of the lattice strain induced by the presence of hydrogen in the metal lattice. Such strain creates an energy barrier that needs to be surmounted in order for the hydride to form or decompose.[79] One way to engineer the extent of the hysteresis is typically to alloy the host metal with a second element, as for example in Pd-Au, Pd-Ag, and Pd-Ni alloys.[80-82]

3.1 Nanoplasmonic hydrogen sensing using metal hydrides

Since the first report (more than 100 years ago[83]) that Pd can absorb hydrogen, it remains one of the most well studied materials regarding hydrogen uptake/release thermodynamics and kinetics, which is motivated both from the fundamental and applications point of view (e.g. hydrogen storage[18]). As for any metal, the dielectric properties of Pd are sensitive to the concentration of absorbed hydrogen, and the bulk Pd-H system has a well known phase diagram, electronic structure, and related optical properties for both metal and hydride phases.[77] Another reason for Pd being an attractive model system is the fact that hydride formation in Pd occurs at convenient experimental conditions such as pressures below 1 bar at temperatures around room temperature.

Recently, the interest in studying the Pd-H thermodynamics and kinetics by means of nanoplasmonic sensing has advanced from conventional thin films and arrays of Pd nanostructures to the single particle level, in order to be able to investigate minute length scale effects on the storage properties. However, the investigation of a small Pd nanoparticle on its own is complicated by its low scattering efficiency, and by large intrinsic damping that broadens its resonance profile[41] and prohibits the use of dark-field scattering spectroscopy otherwise typically used for single particle experiments. These issues may be overcome by the concept of the plasmonic nanoantenna, which can significantly enhance nanoscale optical effects. The principle is that the antenna unit should be able to detect changes experienced by the nanoparticle of interest. In case of H_2 absorption in a Pd nanoparticle, there are two pronounced effects, namely, alterations in both structural (lattice expansion) and electronic properties (change in dielectric function) of the nanoparticle.[61] These changes can be detected through the coupling between the plasmonic antenna and the hydrogen-absorbing particle. First attempts on single particle sensing of the hydrogenation process by means of nanoplasmonics have been shown by Liu *et al.*[75] and Shegai *et al.*[76] Both studies were aimed at lithographically fabricated single Au-Pd heterodimer arrangements such as Au triangle – Pd disc and Au cone with Pd or magnesium (Mg) particle on top, respectively. Although the two approaches demonstrated powerful constructions of well-organized nanostructures at surfaces, their main drawback is that the obtained nanoparticles are polycrystalline and that their surfaces/shapes are rather ill defined.

For a better understanding of the role of particle specific features in the hydride formation/decomposition process, it is therefore useful to employ wet-chemical synthesis of (single-crystalline) nanocrystals[84] that allows fine tuning of the size, shape and crystal facets of the particle of interest. First steps in this direction were shown recently in the studies of ensembles[85] and single[27] Pd nanocubes, where the authors directly probe them using a luminescence technique in the first case, and electron energy-loss spectroscopy in environmental TEM in the second case. Both studies raise interesting questions regarding the influence of nanocube size on the hydride formation phase transition, however in an unusually large particle size regime, i.e. cube sizes between 14-110 nm and 13-29 nm in the respective studies.

Strong size effects are typically expected and have also been experimentally observed for Pd nanoparticles smaller than 10 nm. At these length scales one of the key factors resulting in the dependence of the thermodynamics on the particle size is surface tension, which gives rise to a decrease of the H binding energy via compression of the Pd lattice as nanoparticle size decreases[86]. Moreover, for such small nanoparticles the fraction of atoms that reside on corners or edges is significant. These atoms are more loosely bound and therefore characterized with the higher reactivity toward hydrogen.[87] The effects of decreasing Pd nanoparticle size on hydrogen storage properties have been studied for sizes that range from 1.8 nm to 8 nm. Various effects were observed including: a decrease in width of the plateau[88-90], increased slope of the plateau[88], decreased hysteresis[91] and faster kinetics[92]. Importantly I may note here, however, that all these studies were done for ensembles of nanoparticles.

4 NANOFABRICATION

Nanofabrication is the process of making functional structures with at least one dimension that has the size of 100 nm or less. Ever since it has evolved from microfabrication, a large number of different nanofabrication methods have been developed. Generally, one can distinguish two fabrication approaches known as "top-down", when bulk material is cut, milled and shaped into desired nanostructures with the help of externally controlled tools; and "bottom-up", where nanostructures are built using chemical and physical properties of atoms, molecules or colloidal particles to self-assemble into useful conformations. These two approaches in turn can be divided into three major classes in terms of patterning the final structure: pattern writing, pattern replicating and self-assembly techniques. Each of these classes will be briefly described below.

4.1 Pattern writing techniques

These techniques allow "writing" of the structures on the surface with high flexibility in terms of structural shapes and patterns. Charged beams of ions (in focused ion beam (FIB) lithography) or electrons (in electron beam lithography (EBL)) can be focused into extremely small volumes to perform structuring of the bulk material either by exposure of energy-sensitive polymer resists or by removing material directly. The current resolution limit of these two methods is of the order of 5-30 nm. In scanning probe-based lithographies (SPL), which include several techniques (e.g. lithographies based on STM, AFM, spin-polarized STM and dip pen nanolithography (DPN)), the microscopic or nanoscopic stylus moves mechanically across the surface to form structures with sizes less than 5-10 nm. In some cases with SPL it is possible to manipulate individual atoms. The key limitation of these pattern-writing techniques is a very low throughput, which is accompanied by expensive and complicated equipment. [93]

4.2 Pattern replicating techniques

The uniting feature of these methods is that they all use templates or masks in order to reproduce predefined micro/nanostructures. In photolithography (PL) the mask is patterned by photon energy into a layer of photoresist coated on the substrate surface, which is then developed to form planar structures. Nano imprint lithography (NIL) is a method where nanopatterns are created using mechanical deformation of imprint resist

(typically, nanoimprinting polymers can be cured by heat or UV light) and subsequent processes that remove excess material (e.g. demolding or etching). In ion projection lithography (IPL) and electron projection lithography (EPL), a broad ion (hydrogen or helium) beam or electron beam is projected through a stencil mask to expose the resist material. As opposed to pattern writing techniques, these methods are characterized with high throughput of structured surface. Their resolution limits are quite reasonable and steadily pushed forward (currently, well below 100 nm). However, these methods have low flexibility if tuning of the structure parameters is required, because every new configuration has to be done with a new mask or template. For example in IPL, the masks are also difficult to make, to inspect and to repair. [93]

4.3 Self-assembly techniques

The previously described two methods are top-down methods, and the available fabrication tools always limit their resolution. On the other hand, self-assembly techniques employ nature's own ability to produce extremely complex living organisms "from scratch" by self-organization and self-construction. The aim of these techniques is first of all to achieve nanostructures in true nanoscale (molecule level) and secondly (and as important as first) at low cost. According to a classification made by Zhirnov *et al*[94]:

- chemical self-assembly covers molecular-scale ordering of compounds with precisely designed atomic architectures into more macroscopic structures;

- physical self-assembly concerns the ordering of atoms resulting from physical deposition processes such as molecular beam epitaxy (MBE) or chemical vapor deposition (CVD);

- colloidal self-assembly refers to the processes by which nanoparticles aggregate into clusters within tens of nanometer to tens of micrometer range.

In this thesis, two types of nanostructures were studied: the ones nanostructured via colloidal lithography and the ones made by wet-chemical synthesis. These techniques will be discussed in the following sections.

4.3.1 Colloidal Lithography

A large part of this thesis was dedicated to the development of nanofabrication methods that are based on colloidal self-assembly or rather, colloidal lithography (CL) in order to be able to build dimeric plasmonic nanostructures with a catalyst nanoparticle in the hot spot. CL uses particles synthesized via wet chemistry (e.g. emulsion polymerization or sol-gel synthesis). These colloidal particles are characterized by their ability to form large surface area 2D or 3D arrays with a certain level of order: from highly ordered closely packed patterns (often referred to as "colloidal crystals") to sparse monolayers with short-range order. These particle patterns can be used for the development of evaporation or etching masks. CL has

attracted much attention due to its relative processing simplicity, low cost and impressive flexibility. The resulting patterns can be controlled by simply varying colloidal particle size, separation and processing conditions. Colloidal particles may be synthesized with desired chemical or physical properties, in order to functionalize them for intended purposes. Processing of CL patterns has little need for advanced and expensive tools. The parallel nature of the self-assembly process also makes it suitable for patterning large sample areas (~ cm^2). The feature size of resulting nanostructures can be obtained with resolution of few tens of nanometers, as well as several shapes that are not trivial to produce with EBL can be easily achieved (e.g. cones, hollow cylinders or rings and crescents). All these factors make CL a versatile and cost-effective nanofabrication method. [93-96]

4.3.1.1 Hole-mask colloidal lithography

Hole-mask colloidal lithography (HCL) is a CL variation developed by Fredriksson *et al*.[97] The essential feature of this method is the presence of a sacrificial layer on the substrate surface prior to deposition of colloidal particles. A thin film layer evaporated on top of the colloidal particles (which are subsequently removed) has motivated the name "hole-mask" for this method. The hole-mask is used for evaporation and/or etching that defines parameters of the final structure, and then it is removed with the help of the sacrificial layer. HCL allows nanofabrication with a broader range of materials and material combinations, and a variety of new nanoarchitectures that can be easily realized (compared to other versions of CL, e.g. nanosphere lithography (NSL) and sparse colloidal lithography (SCL)). [97,98]

The specific HCL fabrication steps utilized in this thesis to prepare nanostructures on a substrate are briefly summarized below and accompanied with a sketch for each step (Figure 8):

Step 1: Substrates are cleaned with step-by-step sonication in acetone, isopropyl alcohol (IPA) and methanol. ***Step 2***: Clean substrates are spin-coated with poly(methyl methacrylate) (PMMA) and then soft baked on a hotplate. ***Step 3***: The substrate with the thin PMMA layer is etched shortly in oxygen plasma in order to reduce the hydrophobicity of the surface. ***Step 4***: Water-suspended positively charged polyelectrolyte (poly diallyldimethylammonium (PDDA)) is dispersed on the surface. The substrate is then rinsed with de-ionized water to remove excess of PDDA, and dried with nitrogen flow. PDDA thus forms a very thin positively charged layer on the PMMA surface. ***Step 5***: A colloidal suspension of negatively charged polystyrene (PS) particles is deposited on the surface. Here, the chosen size of the PS particles dictates the diameter of the hole-mask and, consequently, the final fabricated structures. Electrostatic repulsion between the PS particles and attraction between PS and the PDDA-treated surface, respectively, creates an amorphous (no long-range order) PS nanoparticle array. ***Step 6***: A thin film of a material, which is resistant to reactive oxygen plasma etching (typically Au or chromium (Cr)), is evaporated to form the mask layer (10-20 nm thick). ***Step 7***: After mask deposition, the PS particles are "stripped" away with tape, which leaves nanoholes in the plasma-resistant film layer

("hole-mask"). ***Step 8***: Reactive oxygen plasma etching is applied to selectively remove the exposed PMMA layer below the holes. The etching creates a partial undercut in the PMMA as clearly seen in the corresponding SEM image in Figure 8f. The depth of the undercut varies with applied etch time and also depends on the size of the PS particles used. ***Step 9***: At this stage, the processing route of HCL can take different directions in order to achieve various nanostructure shapes. For example, nanodiscs can be obtained by simply depositing material through the hole-mask at normal incidence (Figure 8a). Nanocones can conveniently be made if the evaporation is continued until the holes in the mask completely close due to the shrinking of the hole as material is deposited on the rims of the holes (Figure 8b). Nanodisc dimers are obtained by evaporation of the material at two opposite angles from the surface normal (Figure 8c). Note, that due to the hole shrinking when material is deposited on the edges, in this case, it will result in uneven size distribution of nanodiscs in each pair. In order to have even size of the discs in each pair, the angle of evaporation has to be alternated every 5 nm of deposited material.

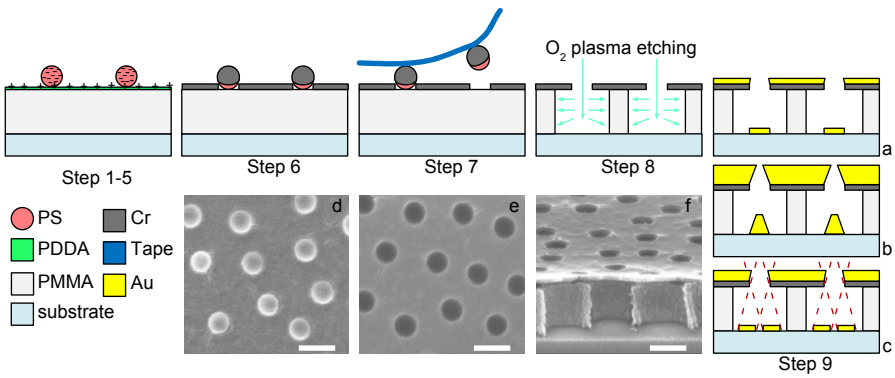

Figure 8. *Schematic illustration of the generic HCL evaporation mask fabrication steps 1-8. The possible routes after these initial 8 steps in HCL are to, for example, either make: (a) nanodiscs, (b) nanocones or (c) nanodisc dimers in step 9. (d) Top view SEM image of the sample structure before and (e) after tape stripping. (f) SEM image of the sample cross-section after plasma etching showing the characteristic under-etching of the PMMA resist layer. The scale bar in all SEM images is 200 nm.*

4.3.1.2 Shrinking-hole colloidal lithography

Shrinking-hole colloidal lithography (SHCL) is a new variation of CL that I have developed and is covered in full detail in the appended Paper I. In brief, SHCL utilizes the effect of the shrinking hole that arises from deposition of the material through the holes in the mask prepared by HCL. When material is deposited through the holes in the mask, it builds up not only on top of the mask but also on the rims of each hole, thus causing the shrinking of the holes in the mask layer. Three approaches were developed in order to achieve the shrinking-hole effect and these utilize sacrificial materials such as C and Cr. These strategies are described below:

C cone approach

This approach is illustrated on the example of an initial Au nanodisc dimer structure (prepared by HCL), to the gap of which a catalyst particle (e.g. Pd) is delivered. ***Step 10***: C is e-beam evaporated at normal incidence through the hole-mask and forms a cone due to the successive shrinking of the nanoholes of the mask upon C deposition onto the rims of the hole. The rate and the thickness during C evaporation are carefully controlled to make sure that the holes in the mask do not close completely in order to provide enough space for subsequent deposition of the material that will form the particle to be delivered to the antenna hot spot. ***Step 11***: the particle material (here, Pd) is deposited directly after C at normal incidence through the small hole that is left from the previous step. In this way it forms a small particle on top of the sacrificial C cone structure (Figure 9a). The diameter of the particle is controlled by the thickness of the evaporated C layer (cone height). Evaporating C and/or particle material at a small angle from the normal will, additionally, result in a tunable lateral particle position (Figure 9 e&f vs. g&h). ***Step 12***: the sample is placed in acetone to dissolve the PMMA layer in a lift-off together with all the excess material on top. ***Step 13***: the sacrificial C cone is etched away in mild oxygen plasma. The oxygen radicals thereby attack the C cone uniformly from all directions, such that the particle is delivered into the gap of the gold dimer as illustrated in the sequence of SEM images in Figure 9a-d. The C cone approach works well for delivering the particle of interest into the gap of the nanodisc dimer. The drawback (or equally advantage if an oxide particle is to be delivered) of this method is that oxygen plasma etching, which is used to remove the C, also may oxidize the particle or nanoantenna material (for example when Ag is used).

Cr cone approach

In order to eliminate the above-mentioned issues related to unwanted oxidation, Cr can be used as an alternative sacrificial nanostructure material in a second version of SHCL. To illustrate this approach, instead of an Au nanodisc dimer, a single Au nanodisc is used as the initial nanoantenna structure. ***Step 10:*** as shown in Figure 10a, Cr is deposited at normal incidence instead of C to form the sacrificial cone structure. In this way the diameter of the hole in the mask, and thus the size of the final nanoparticle, can again be finely adjusted via the hole-closing effect. ***Step 11***: the material to form the second particle is deposited at an angle from the normal (to avoid deposition onto the Cr cone) through the tuned hole-mask to be delivered to the close vicinity of the antenna disc (Figure 10b). Tuning of the particle evaporation angle will yield various particle positions relative to the Au nanodisc. Alternatively, if e.g. a nanodisc dimer is the initial antenna structure, one would deposit the Cr cone at an angle and then the particle material at normal incidence to deliver the particle to the dimer hot spot. ***Step 12***: the PMMA layer with excess material on top is removed by lift-off in acetone. ***Step 13***: the Cr cone is removed by dipping the sample in a liquid Cr-etch, leaving only the antenna with a particle in the hot spot on the surface (Figure 10c).

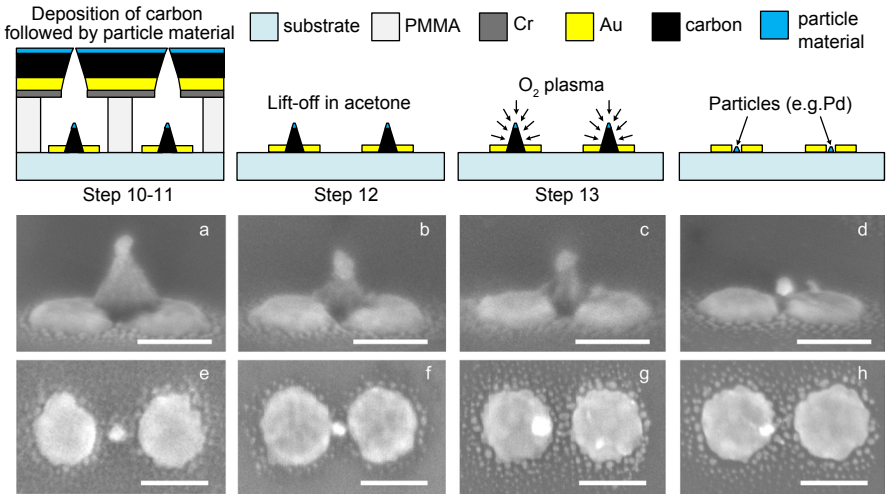

Figure 9. *Schematic illustration of the first SHCL nanofabrication strategy used here for placing a small Pd particle in the gap of an Au nanodisc dimer by using a C cone as the sacrificial particle transfer structure. (a-d) 70° tilted SEM images of a sample made on a Si wafer substrate after 1, 2, 3 and 4 minutes in oxygen plasma, respectively. Clearly, the homogeneous removal of the sacrificial C structure by the oxygen plasma is seen with the consequent "delivery" of the Pd particle in the antenna gap. (e&f) SEM images of Au nanodisc dimers with different gap sizes and with a Pd particle in the gap. (g&h) SEM images of Au nanodisc dimers with a gap of 30 nm, and with small Pd particles with two different sizes (21 nm and 10 nm) placed at different lateral positions and in the gap. The scale bar in all SEM images is 100 nm.*

This second SHCL approach, which exploits a sacrificial Cr cone, is very efficient and straightforward to implement. However, also in this case there are a number of limitations in the range of materials that can be used for nanoantenna structure and particle material, dictated by the compatibility with Cr-etch. Moreover, concerns may arise about possible contamination of the sample (e.g. when catalytic/chemical processes on the formed particle are of interest) from the wet etch step.

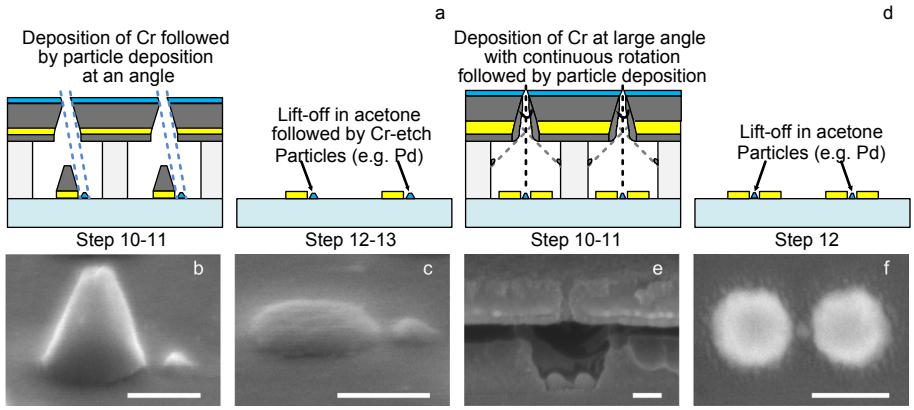

Figure 10. *Schematic illustrations of the second (Cr-cone, left) and third (Cr-funnel, right) SHCL nanofabrication strategies used here for placing a Pd nanoparticle next to an Au nanodisc antenna or in the gap/hot spot of an Au dimer, respectively. (a) Sacrificial Cr-cone strategy: Cr is deposited at normal incidence to shrink the hole in the mask and forms a cone on top of the Au antenna. When the desired hole-size has been reached, the second particle (here Pd) is deposited through the mask at a small angle from the normal. After lift-off to remove the mask, the sacrificial Cr cone is removed using a liquid Cr-etch. (b) SEM image of a Cr cone with an Au nanodisc underneath and a small Pd particle next to it. (c) SEM image of an Au nanodisc and smaller Pd particle next to it after the Cr-etch step. (d) Sacrificial Cr-funnel strategy: Cr is deposited at a large angle form the normal with continuous sample rotation to form a funnel while shrinking the hole in the mask. In this way the Cr is deposited only onto the mask and onto the walls of the (underetched) PMMA resist layer in the hole, i.e. no Cr is deposited onto the sample surface. Therefore all the excess material can be removed directly during the final lift-off and no reactive or wet etch is required. (e) SEM image of a sample cross-section before lift-off. The sample features Ag nanodisc dimers with a Pd particle in the gap. (f) Representative SEM image of an Au nanodisc dimer with a Pd particle in the gap fabricated using the Cr funnel approach. The scale bar in all SEM images is 100 nm.*

Cr funnel approach

As a solution to overcome all the concerns with the previous two approaches, there is a third option that as the only additional requirement relies on an e-beam evaporation system, which features sample tilt and rotation simultaneously during deposition. In this way it is possible to eliminate any etching step by again employing Cr to grow a sacrificial structure to tune the diameter of the hole in the mask. Now, however, it is deposited onto the hole-mask at a large angle and with continuous rotation of the sample. In this way, owing to the significant under-etching of the PMMA in the hole-mask, a Cr funnel structure is grown around the nanoantenna in the hole (Figure 10e). The Cr is deposited until the hole in the mask decreases sufficiently for the desired

diameter of the particle to be delivered to the antenna (***step 10***) and then the particle material is deposited through the remaining hole either orthogonally to the surface or at an angle to control the lateral position with respect to the nanoantenna (***step 11***). Given that the angle of Cr evaporation is chosen appropriately (which exact angle to use depends on the size of the initial hole of the hole-mask and on the PMMA thickness), it will be deposited only on the walls of the PMMA layer (i.e. not onto the sample surface itself), such that all the sacrificial material can be removed directly during the lift-off in acetone (***step 12***), and without having to use the Cr-etch at a later step. Hence, any incompatibilities with oxidation-sensitive or non-wet-etch-resistant materials are completely eliminated, as well as the risk for contamination. At the same time the impressive flexibility to build complex polymaterial nanoantenna structures in a completely self-aligned way is retained.

In this way, by exploiting sacrificial materials that are deposited in order to shrink the hole in the mask and then are removed afterwards, it is possible to fabricate complex nanostructures consisting of several nanoparticles of different materials and/or of different sizes. See, for example, a selection of nanostructures that can be fabricated with the SHCL method in Figure 11. In addition, the method is self-aligned in nature and thus allows precise control over the particle sizes and the distances between the particles (i.e. gaps). Since the method is a derivative of the HCL method, it preserves the ability of patterning large areas (few cm^2) with aligned complex nanostructures.

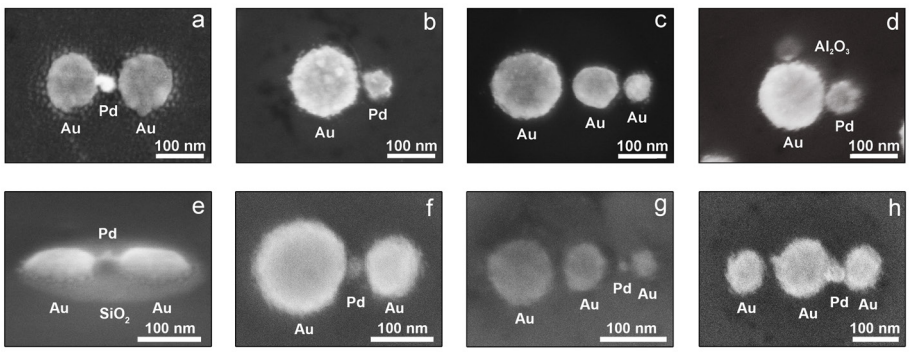

Figure 11*. A selection of nanostructures that can be made with SHCL: (a) an Au nanodisc dimer with a Pd particle in the gap; (b) an Au nanodisc with a smaller Pd particle on its side; (c) a cascaded Au nanodisc trimer; (d) an Au nanodisc with a smaller Pd and aluminium oxide (Al_2O_3) particle on each side; (e) an Au nanodisc dimer covered with a thin silicon oxide (SiO_2) layer (deposited by chemical vapour deposition) prior to placement of a small Pd nanoparticle in the dimer gap; (f) an asymmetric Au nanodisc dimer with a small Pd nanoparticle in the gap; (g) a cascaded Au nanodisc trimer with a small Pd nanoparticle in one of the gaps; (h) a symmetric Au nanodisc trimer with a small Pd nanoparticle in one of the gaps.*

4.4 Wet-chemical synthesis of metal nanoparticles

This section concerns fabrication methods that are completely different from the ones discussed previously in this chapter. The discussion here is about the growth of solid metal nanoparticles via chemical reactions in a liquid reaction medium. The two approaches, i.e. "top down" and "bottom up", discussed in the beginning of the chapter, are also applicable to the wet-chemical synthesis of colloidal metal particles. The first one involves breaking down bulk metals to obtain metal particles, which have to be stabilized with protecting agents in order to preserve the obtained particle shape and avoid aggregates. The method is versatile for fabrication of a wide range of metal colloids, however, it requires complicated machinery that is difficult to adjust so that narrow particle size distributions can be achieved. The second, "bottom up" approach, which is more widely used, involves the following methods:

1) *Chemical reduction of metal salts*, which is done at the embryonic stage of the nucleation to obtain metal atoms of zero valences that can collide in solution with further metal ions/atoms/clusters and form irreversible "seeds" of stable metal nuclei.

2) *Electrochemical synthesis* of metal nanoparticles comprises several steps, which involve oxidative dissolution of a sacrificial bulk metal anode to metal ions that reductively form zero-valent metal atoms at the cathode, and then proceed to further form metal particles via growth and nucleation.

3) *Controlled decomposition of metastable organometallic compounds* is associated with the transition metals. Both organometallic complexes and, in some cases, the organic derivatives of the transition metals can be decomposed into short-lived nucleation particles of zero-valent metals with the help of heat, light or ultrasound. The nucleation particles are then stabilized using colloidal protective agents.

4) *Preparation in micelles, reverse micelles and encapsulation*, is related to the use of colloidal self-assemblies (e.g. micelles, water-in-oil reverse micelles, vesicles), which serve as amphiphilic "microreactors" to trap metal ions that upon introduction of reducing agents can form metal particles.

Similar to the "top down" case, a variety of stabilizing agents (e.g. donor ligands, polymers and surfactants) has to be applied to the "bottom up" produced nanoparticles, in order to control their growth and to prevent agglomeration. There are two distinguished modes of particle stabilization, i.e. *electrostatic* and *steric*. Electrostatic stabilization employs Coulomb repulsion between particles, which is caused by electric double layer formation of species (e.g. carboxylates, polyoxoanions) adsorbed at the particle surface and the corresponding counterions. Steric stabilization is usually achieved by the use of macromolecules (e.g. polymers, oligomers) that adsorb on the particle surface and thus provide a protective shield. There is also a third mode of stabilization, which is the combination of the above two modes and is called *electrosteric* stabilization. It is achieved by the use of ionic surfactants that are

characterized by a polar head group capable to create an electric double layer, and a lypophilic chain that provides steric repulsion.

Wet-chemical synthesis is a powerful toolbox to obtain nanoparticles of wide material, shape and size (down to 1-100 nm) range in both water (hydrosols) and organic solvents (organosols). Prepared nanoparticles can easily be dispersed on supports to be able to characterize them via microscopy techniques, and to use them in various studies. The main concern with wet-chemically synthesized nanoparticles is that experiments have to be carefully designed and take into account the presence of surfactant molecules covering the particle. The surfactant might hinder the activity or cause unwanted response of the particle by "blocking" the surface. Thus, it is important to establish proper cleaning procedures, which help to remove surfactants, but at the same time enable preservation of particle properties (e.g. shape, size, activity, etc.). [99,100]

The Au-Pd heterodimers investigated in this thesis were made using electrostatic self-assembly by our collaborators in the Moth-Poulsen group at Chalmers. Whereas plasmonic Au spheres were purchased from the company (Sigma Aldrich) and used as received, the Pd particles of different sizes and shapes were synthesized by adapting procedures described in the literature[84,101,102]. Briefly, the method for Pd particle synthesis comprised a chemical reduction of the metal salt (hydrogenchloropalladate (H_2PdCl_4)) with ascorbic acid in aqueous solution of a surfactant material (cetyltrimethylammonium bromide (CTAB) or chloride (CTAC)). The Pd seeds obtained this way were further used to make cubes of larger sizes (or other shapes) by means of seed-mediated growth. Figure 12 represents a selection of various heterodimer structures that can be obtained with this approach.

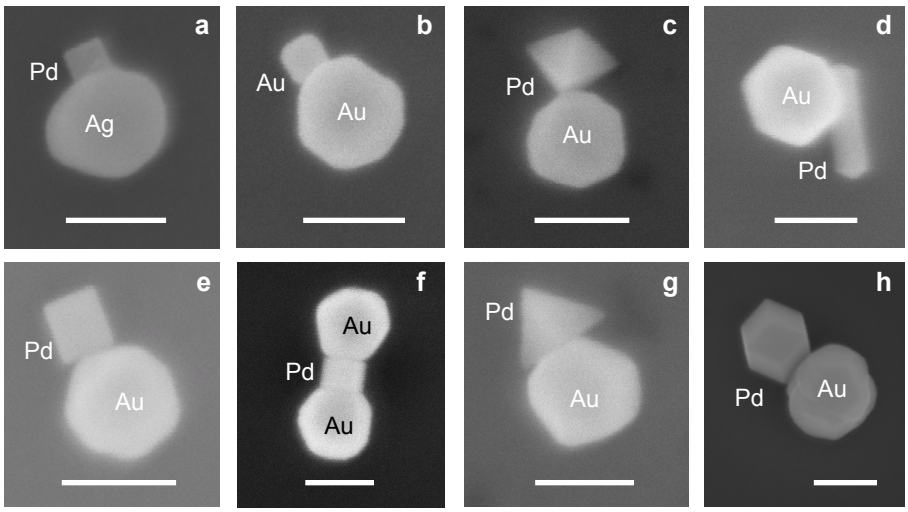

Figure 12. *A selection of the heterodimer structures that can be made via wet-chemical synthesis: (a) an Ag sphere with a Pd cube; (b) an Au sphere with an Au cube; (c) an Au sphere with a Pd octahedron; (d) an Au sphere with a Pd rod; (e) an Au sphere with a Pd cube; (f) two Au spheres with a Pd cube in-between; (g) an Au sphere with a Pd tetrahedron; (h) an Au sphere with a Pd dodecahedron. The scale bar in all the SEM images is 100 nm.*

5 FABRICATION TOOLS

As was discussed in the previous chapter, the nanostructures were produced by implementing a new SHCL method, which was developed from the generic HCL platform. These two methods involve various processing techniques, and this chapter gives an overview of the tools and processes that were used.

5.1 Spin coating

Spin coating makes it possible to achieve uniform films of a viscous material (e.g. polymers) on the surface of the substrate with well-controlled thickness. In spin coating, typically, few droplets of a fluid (usually a solution of polymer in a solvent or a suspension of a solid) are deposited on the centre of the substrate and then it is rotated at a high speed. The rotations make the fluid spread by centrifugal force to the edges of the substrate, and eventually a uniform thin film is formed on the surface. Film thickness and quality of the coated film depend on the material of the fluid (composition, viscosity, wetting, solvent evaporation rate), properties of the substrate (surface roughness, wetting) and conditions of the spinning process (spin speed, acceleration time, exhaust conditions).

The next step after dispensing is acceleration in the typical speed range of 1000-6000 rpm. The exact speed should be chosen considering the properties of both fluid and substrate. Other factors that affect evaporation rate and consequently, film thickness, are turbulence and ambient humidity. Spinning is usually performed in a closed spinner bowl environment to reduce the effect of airflow around the spinning substrate and also to maintain full exhaust during the spinning. After spinning, the substrate is usually baked at temperatures in the range of 100 to 250°C to remove the solvent and to leave only the film of the resin material on the surface.[103]

5.2 Plasma etching

Plasma can be considered as a fourth state of matter along with solid, liquid and gas, although its properties are similar to the gas state. Plasma consists of atoms, molecules, radicals, ions, neutrals and free electrons. It is locally polarized but the number densities of positive and negative charges are equal on average. In micro- and nanofabrication plasma is widely used for deposition and etching processes.

In this thesis, all plasma processes were performed in the commercially available system Plasma Therm BatchTop PE/RIE m/95. It is a reactive ion etching (RIE) system that operates at radio frequency (RF 13.56 MHz) and has a maximum power of 500W and pressure up to 500 mTorr. The main chamber is pumped by a turbo pump and a mechanical roughing pump. Inside the chamber there is a bottom electrode (cathode) where samples are placed. The cathode is capacitively coupled to a radio frequency (RF) generator and is water-cooled. The top electrode (anode) and the chamber walls are grounded. The plasma is generated by applying glow discharge between two electrodes to the gases that are supplied through the gas inlets. The process gases include O_2, CF_4, Ar and H_2. Strong electromagnetic field causes the gas molecules to be stripped of electrons and become ionized, and thus, plasma is created. After plasma ignition, due to the fact that electron mobility is much higher than the mobility of ions, the cathode acquires negative charge and the sample placed on top of the cathode is exposed to positive ion bombardment. At the same time there are also plasma-generated reactive species that diffuse and adsorb on the surface of the sample, where they form highly volatile compounds. The volatile reaction products are desorbed into the gas phase. This process is greatly accelerated by ion bombardment via sputtering. The volatile reaction products are then pumped out from the system. Thus, the etching in plasma system occurs simultaneously via two mechanisms: physical – by ion bombardment, and chemical – through the chemical reaction between sample material and reactive species of the plasma.[98,104,105]

In this thesis O_2 plasma etching was used in order to remove the sacrificial polymer layer utilized for sample fabrication with HCL, as well as for removal of sacrificial C cone structures in SHCL. As mentioned earlier, it can be quite a harsh process that can change properties of materials exposed to it. Care should be taken in the duration of etching with O_2 plasma since it may oxidize the particles such as Pd or Pt, which is not desirable if the oxide cannot be removed without harming the entire structure. For example, as can be seen from SEM images taken from the synthesized Pd cube before and after O_2 plasma cleaning (Figure 13), long exposure times can affect the surface of the particle. In this case the appropriate cleaning procedure to remove/reduce the oxide could be for example flushing the sample with H_2 gas at slightly elevated temperature.

H_2 plasma etching was utilized for cleaning the wet-chemically synthesized particles from surfactant material covering the particles used in this work.

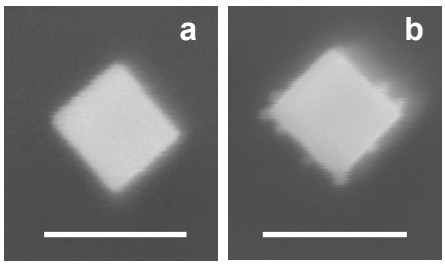

Figure 13. *SEM images of a synthesized Pd cube (a) before and (b) after 7 min of O_2 plasma treatment. The small features that appear are presumably indicators of oxidation. The scale bar in the SEM images is 100 nm.*

5.3 Vacuum deposition of materials

Vacuum deposition is a physical vapour deposition (PVD) process. The source material is heated thermally, which causes atoms or molecules from the source to travel directly to the substrate where they form a thin film of vaporized material by re-condensing on its surface. The vacuum conditions allow the particles to reach the target sample without (or very few) collisions with residual gas molecules in the deposition chamber. Such a process requires a good vacuum in order to obtain a long mean free path between collisions; although, at such pressure there is still a lot of residual gases that can contaminate the film by impinging on the substrate during deposition. In order to get films with high purity it is important to use high (10^{-7} Torr) or ultrahigh ($<10^{-9}$ Torr) vacuum.

The thermal vaporization source is one of the simplest sources to produce vapours of materials. As the name suggests, it's a source where thermal energy is used to produce the vapour of the deposited material. There are several common heating techniques for such evaporation, which include resistive heating, high-energy electron beams, low energy electron beams, and inductive heating. In this thesis, resistive heating and e-beams were used and these techniques will be described below.

5.3.1 Resistively heated sources

Materials that vaporize at temperatures below 1500°C can be heated to sufficiently high temperatures by passing high electric current through a filament container (with source material), which has finite electrical resistance. There are several requirements to such an evaporation source. First of all, the source simply has to be able to contain the source material and prevent it from falling from the heated surface. The reason is that many materials become liquid at the temperatures that are required to get reasonable deposition rate. Typically, for such purpose the source has a form of a container (crucibles, boats, baskets, wires, etc.) and can also have a wetting surface, which allows good thermal contact between the hot surface and the material being vaporized. There are also other materials that instead of evaporating get sublimated

(e.g. Cr, C, Mg, Pd, cadmium (Cd), arsenic (As)), which means that they don't melt or flow, and for such materials a rod type source can be used or the evaporant material can be in powder or tablet form, which in turn is placed in suitable container. Another requirement for the source is that it has to provide thermal energy to the evaporant at high temperatures without extensively vaporizing itself. Finally, the most important requirement is that the source has to be compatible with the evaporant, which means that no extensive chemical reaction or alloying between the source and the evaporant material is acceptable. Most common materials that are used as resistively heated sources are tungsten (W), tantalum (Ta), molybdenum (Mo) or C, which are known to have the highest melting points and lowest vapor pressures among elements. High current connections to the source are usually made of materials that have high electrical conductivity (e.g. Cu).[106,107]

In the early stages of this thesis work, a commercially available Edwards 306 Evaporator was used for thermal evaporation of the hole-mask and Au nanodimers. The fully automatic turbo-molecular pumping system of the Edwards gives a base pressure of less than 5×10^{-7} mbar. It's equipped with a 4-position resistive evaporation source and has a tilt stage, which allows high precision angle evaporation. The sample is placed upside down on tiltable stage facing the evaporant source, which is heated. An almost uniform film of material is evaporated all over the chamber including the sample position.

5.3.2 Electron beam heated sources

Electron beam evaporation involves intense high-energy e-beams and it allows a wide variety of materials to be evaporated at high rate and with minimum consumption of energy. As opposed to resistive heating evaporation, e-beam evaporation can also be used for deposition of materials that evaporate at temperatures above 1500°C such as most ceramics, glasses, carbon and refractory metals, or in cases when a large amount of material is needed to be evaporated.

Electrons are usually generated in a thermionic source or by ionizing gaseous atoms and molecules, which act as a cathode. The evaporation material acts as the anode and it's contained in a crucible that is usually water-cooled. When the e-beam hits the surface of the material electrons start to interact with the atoms of the evaporant. As a result, the kinetic energy of the electrons is converted into various forms of energy, most of which constitutes thermal energy (~85%). The thermal energy produced in this way is used to melt or sublimate the evaporant to achieve a desired vapour pressure. Another advantage of e-beam deposition is that the highest temperature of the evaporation occurs only where the e-beam hits the evaporant surface. Therefore, if the evaporant material can be melted, and a water-cooled copper crucible is used – the melted material forms a "skull" of its own by solidifying itself near the interface of the area that is hit by the e-beam. Thus, the melted material is contained in its own solid "mould", which helps to avoid reaction of the evaporant with the crucible material.[106,107]

As can be seen in some of the SEM images in Paper I as well as in Figure 14 below, there are small particles visible around some of the Au nanodiscs (e.g., Figures 1a and 3a−h of the Paper I). These small particles are Au particles, which are formed most likely due to "splashing" that occurs when evaporated Au atoms/clusters traveling to the sample substrate collide with the edges of the hole-mask, and therefore slightly change their direction and end up off the main target area determined by the hole-mask. It is a characteristic and inevitable feature in the cases when underetching of the mask is present (also, e.g., when EBL double-layer resists are used), however the effect can be reduced to some extent using e-beam evaporation rather than resistive evaporation (Figure 14).

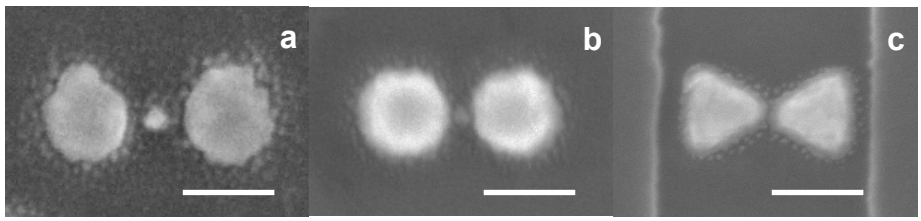

Figure 14. *SEM images of the Au nanodisc dimers made (a) with resistive evaporation and (b) e-beam evaporation. As can be seen the latter technique results in smaller amount of Au "splashes" around the nanodiscs. (c) An SEM image of a pair of Au triangles made by EBL (image courtesy of Joachim Fritzsche), where tiny "splashes" of Au are also visible. The scale bar in all the SEM images is 100 nm.*

6 CHARACTERIZATION TECHNIQUES

6.1 Scanning Electron Microscopy

Scanning electron microscopy (SEM) is a versatile technique that allows imaging of organic and inorganic materials in the nm to μm range. The examined area is irradiated by a focused electron beam, which can be swept across the sample surface in a raster pattern. Several types of signals are generated when the electron beam interacts with the sample: secondary electrons, backscattered electrons, characteristic X-rays, transmitted electrons and specimen currents. The most common operating modes of SEM use the signal from secondary and backscattered electrons to form a high-resolution image of the examined sample area.

Backscattered electrons are high-energy electrons that come from the beam and that get reflected from the sample by elastic scattering. They give information about the chemical composition of the sample as the intensity of the signal is strongly related to the atomic number Z: heavier atoms backscatter electrons more strongly than light atoms and, thus, appear brighter in the image. Secondary electrons are ejected from the outer shells of the sample atoms by inelastic scattering when interacting with the e-beam. They have much lower energy than backscattered electrons and come from within few nanometers of the sample surface and, thus, give good topographic information. The three-dimensional-like image of the sample is obtained due to the large depth of field of SEM (i.e. how much of the object under observation remains in focus at the same time) and the good contrast between backscattered and secondary electrons.

For conventional SEM imaging there are several requirements. Besides being of reasonable size to fit in the SEM chamber, samples should be conductive, at least at the surface, in order to prevent charge accumulation. Another requirement is vacuum condition during imaging to prevent spreading and attenuation of the e-beam. The latter complicates the investigation of samples that vaporize. In both cases when samples are non-conducting or vaporize – they can be covered with a very thin layer of conducting material such as Au, Pt, Cr or C. Another way to solve the mentioned issues is to use Environmental SEM (ESEM) or SEM at low voltages, where no coating is required. In ESEM, the sample is placed in relatively high-pressure environment rather than in high vacuum. In such conditions, the e-beam starts interacting with gas species. This results in positively charged ions, which neutralize negative charges on the sample surface. For SEM at low voltages, typically field-

emission gun (FEG) SEM machines are used, as they allow reasonable brightness and contrast at low accelerating voltages. [108]

In this thesis, all samples for single particle spectroscopy were fabricated on pieces of a thermally oxidized Si wafer with the thickness of the oxide being 50 nm. The presence of the thin oxide layer was crucial in order to perform dark field scattering spectroscopy and is explained in the Section 6.2.1. The oxide layer on the substrate was the cause of SEM images having slightly lower resolution, compared to the case if nanostructures would have been fabricated on plain Si. SiO_2 is a non-conducting medium and it results in some charge build-up on the sample surface. However, since it is quite thin, the effect is not as severe as it would be if samples were fabricated on glass substrate (Figure 15). Nevertheless, the image quality was sufficient to identify suitable nanostructures, and make approximate estimations of nanostructure dimensions.

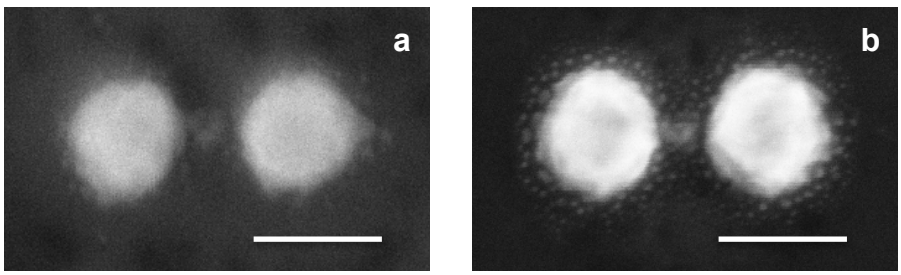

Figure 15. *SEM images of two Au dimer nanostructures with a small Pd particle in the gap made under identical conditions (i.e. in parallel) with the only difference being the used substrate: a) thermally oxidized silicon (SiO_2 ~ 50 nm); b) regular silicon wafer. The nanostructure on silicon is seen with much more detail and with better resolution, as opposed to the one made on the oxidized silicon substrate, where the thin non-conducting layer of oxide causes slight charge build-up and, thus, worsens the image resolution. The scale bar in both SEM images is 100 nm.*

6.1.1 Identification of SEM-imaged nanostructures in the optical microscope

SEM was a key tool in this thesis in order to find and characterize individual nanoantenna structures, which were further used in the single particle plasmonic sensing experiments, thus allowing correlation of measured signals from the nanoantenna structure and nanoparticle of interest with their appearance in SEM. To be able to find identified nanostructures after SEM imaging in the optical microscope, where the plasmonic sensing experiments were performed, the following procedure was developed and used. First, with the aid of a scribing pen the sample was marked with one or two scratches that were clearly visible in the optical microscope. Then SEM imaging was done nearby one of the scratches, however not very close (at about 200-300 μm distance), since a scratch on the sample surface produces a lot of stray light in the optical microscope, which would interfere with the plasmonic nanoparticle

scattering signal if the particle was too close to it. When a suitable nanostructure was found, it was imaged at high magnification in order to be able to clearly see the structural details and estimate the size of the particle. Then the said structure was imaged at several decreasingly lower magnifications in order to create a “map” of the sample topography that would step by step allow finding the particle of interest “from scratch” in the optical microscope. See for example, such a “map” in the Figure 16 for a sample with spin-casted wet-chemically synthesized heterodimers of Ag–Pd, where the map was constructed in order to find the particle depicted in the Figure 17. Each part of the “map” in Figure 16a-d, has some kind of feature that would make it possible to navigate on the sample surface when looking at it in the optical microscope. For example, there is a big scratch mark in the left part of Figure 16a, few dirt pieces in the left lower corner of Figure 16b (which are probably small splinters from the substrate after making a scratch mark), an even smaller piece of dirt in the Figure 16c, and then the ensemble of nanoparticles that create a unique pattern in the Figure 16d, and that can be visible as a corresponding pattern of bright spots in the optical microscope with dark-field illumination in Figure 16e.

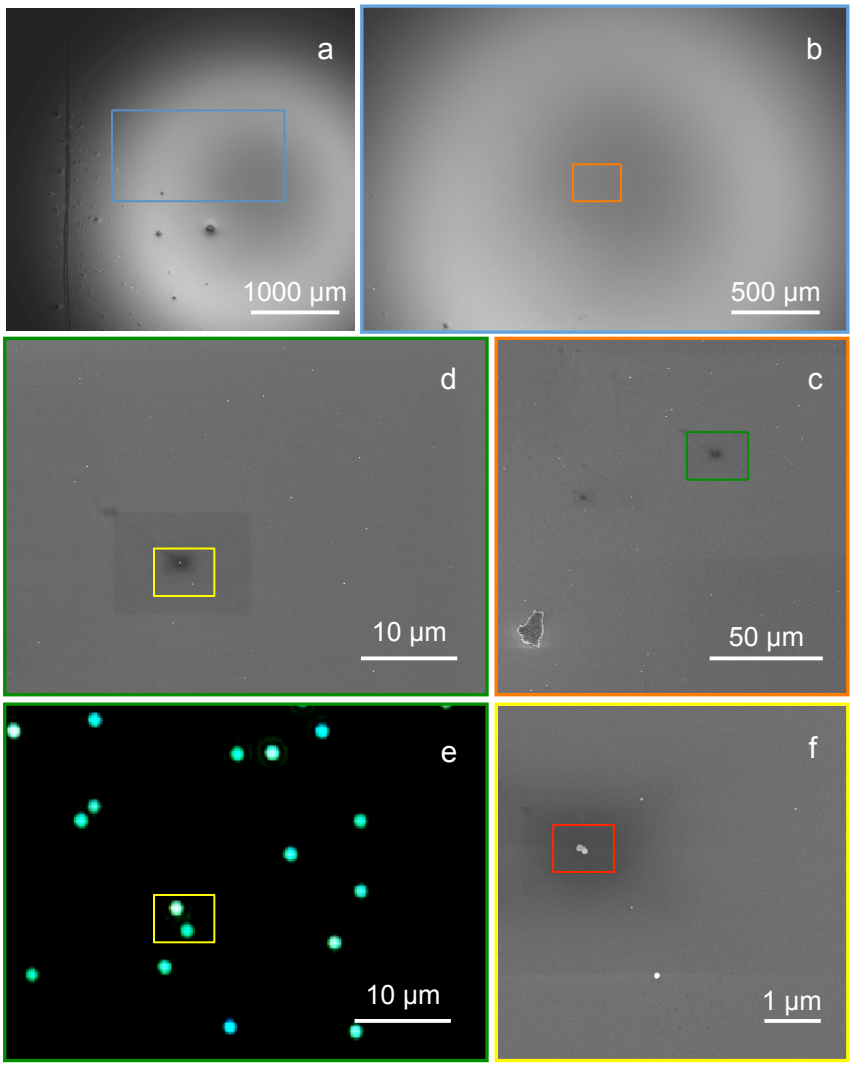

Figure 16. *The "map" for finding a particle in the optical microscope after SEM imaging: a) SEM image at low magnification (145x) of the sample area near the scratch (dark line to the left); b) zoomed in view (235x) on an area marked with a blue square in (a); c) zoomed in view (2000x) on an area marked with an orange square in (b); d) zoomed in view (6000x) on an area marked with a green square in (c); e) optical microscope view of an area depicted in the SEM image in (d); f) zoomed in view (26000x) on an area marked with a yellow square in (d) and (e). Zoomed in view on the particle in a red square (f) can be found in the Figure 17.*

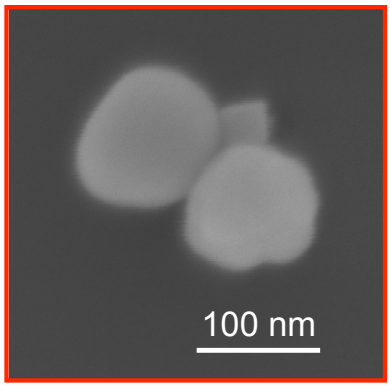

Figure 17. *SEM image of two Ag spheres with Pd cube in between, that can be found with the "map" constructed in Figure 16 and is located in the red square in panel f.*

6.2 Dark-field scattering spectroscopy

Typically, light can be transmitted, absorbed or scattered by a material. Dark-field scattering spectroscopy (DFSS), as the name suggests, is dedicated to the detection of scattered light, and it requires dark-field illumination. For plasmonic nanoparticles, scattering properties are strongly wavelength dependent and are enhanced most at the plasmon resonance frequency. DFSS is a very useful technique for single particle characterization with the aid of plasmonic particles, and it can be performed using a standard optical microscope in dark-field mode. Dark-field illumination implies that the incident light is directed to illuminate the sample and that the detector should not capture any directly irradiated light, except the one scattered by the sample.

Dark-field illumination can be achieved in several experimental configurations, which in turn can be classified as transmission and reflection modes in general terms. In the first case, the specimen has to be transparent to allow transmission of light, and this configuration usually requires positioning of a dark-field condenser with high numerical aperture (NA) below the sample. In this thesis, reflected dark-field illumination or *epi-illumination* was used, where it is sufficient to have a reflected light dark-field objective (that serves both as condenser and objective) and the sample can be opaque. In both illumination cases, the central portion of the cone of irradiated light is blocked; so that the sample is illuminated with a hollow cone of light as illustrated in Figure 18. In transmission dark-field mode (Figure 18a), the high NA dark field condenser focuses collimated illumination light at an angle steeper than can be collected by the objective, which thus gathers only light scattered by the sample.

In the case of dark-field epi-illumination (Figure 18b), the collector transforms the light coming from the microscope lamp into a roughly parallel beam. Most of the light is blocked by the condenser-aperture-diaphragm, which has a central stop, so that only peripheral rays of the beam pass through. The light is then reflected by a 45° mirror

with a circular hole in the centre, so that the light travels to the specimen vertically down on the outside of the actual objective lens. Then the light is focused on the sample by an inner mirror at the end of the objective housing. Light is scattered by the nanoparticles on the illuminated sample surface, and part of it is passed back via the objective lens to the eye-piece. The resulting image constitutes a collection of bright spots of different colours and intensities (depending on the particle shape, size and material) against dark background (hence the name "dark-field"), see, for example, Figure 16e. Notice that in the corresponding SEM image in Figure 16f there is an arrangement of two Ag spheres with Pd cube in between and, slightly lower, there is a single Ag sphere. These two nanostructures appear as two bright dots in the optical microscope image (Figure 16e, yellow square). However, if we look back at the SEM image (Figure 16f) then it is possible to see also three single Pd cubes, which are not visible in the optical microscope due to the fact that Pd doesn't scatter light very efficiently. This is a nice illustration of why a strongly scattering plasmonic nanoantenna unit such as Au or Ag is needed when using DFSS for studying small nanoparticles (< 40 nm), in particular the ones consisting of materials that have poor scattering properties due to high intrinsic absorption. [109,110]

6.2.1 The role of the substrate in DFSS

As was already mentioned in Section 6.1, the use of a conductive Si wafer substrate was crucial in order to be able to characterize the individual nanoparticles in SEM and subsequently correlate the measured signals from these single particles with their appearance (i.e. size and shape). The presence of the thin (50 nm) thermally grown SiO_2 layer on the Si wafer was necessary, in order to perform DFSS. The reason for this is that nanoparticles on the bare Si substrate are simply not visible in the dark-field microscope, due to the fact that a polished Si wafer reflects a lot of light and thus suppresses the signal from the individual plasmonic nanoparticles. Placing a transparent dielectric layer such as SiO_2 on top of the reflective Si substrate gives rise to interference effects[111] between the incoming wave and the wave reflected by the Si substrate. This stems from the different refractive indices of the two materials, which are strongly wavelength dependent. The incoming wave of light undergoes multiple reflections and refractions at the interfaces. The dielectric thickness modulates the phase of light and the interference at the interfaces modulates the intensity of the propagating light. Bilayer substrates of this kind are used e.g. for SERS[112] and for detection of atomic layers of graphene in the optical microscope[113]. The interference effect strongly depends on the thickness of the dielectric layer as well as the incidence angle of the incoming light. The presence of the plasmonic nanoparticle on the surface further complicates the physics behind this phenomenon and will not be discussed here. For my work it was sufficient to use 50 nm SiO_2 to be able to clearly see the plasmonic particles in the optical microscope and measure the scattering spectra from the individual nanoparticle arrangements. However, it will be very interesting in the future to study different effects that arise with changing substrate arrangements (i.e. different reflecting material, different material and thickness of the dielectric, multiple reflecting and transparent layers, the size of the plasmonic particle, etc.).

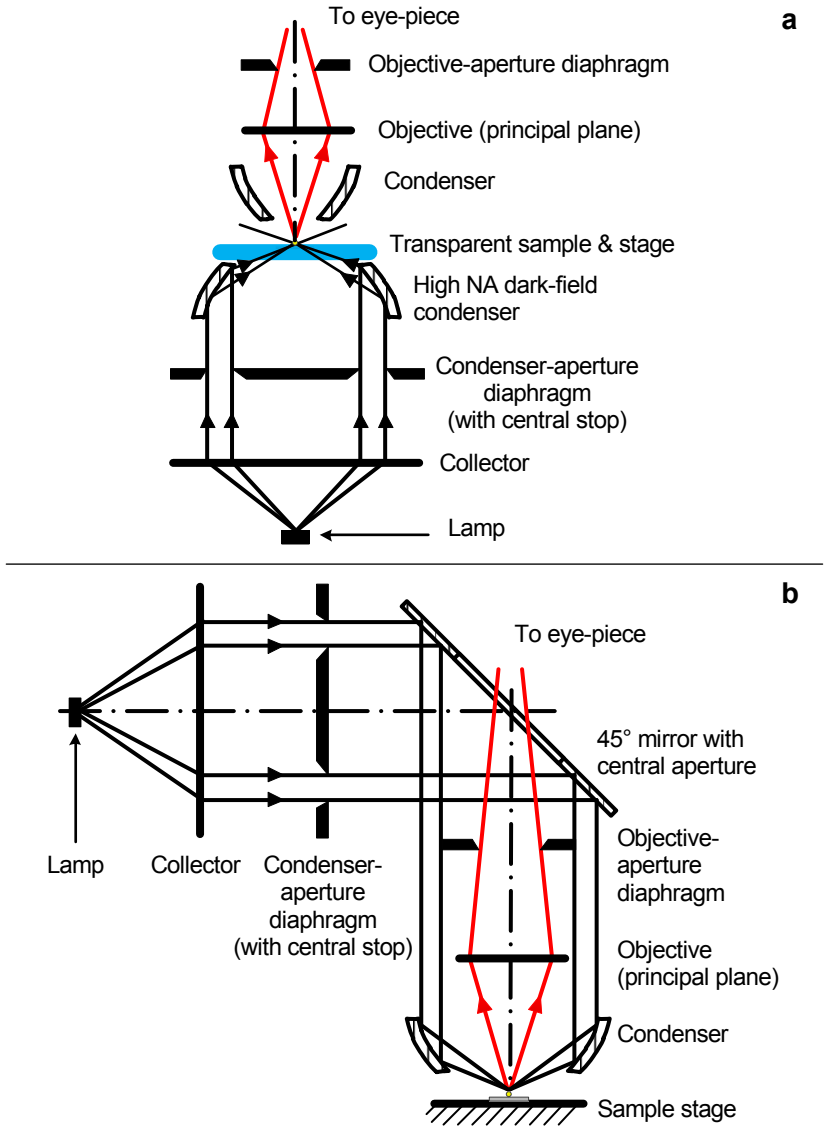

Figure 18. *Schematic drawing of the ray-path in (a) transmitted dark-field illumination with high NA condenser; and (b) reflected-light dark-field illumination with an ellipsoidal ring-mirror reflector (beam-splitter) and a concave ring-mirror condenser. Note that all lenses are only shown as a line indicating their principal plane. Incident light and scattered light are shown as black and red arrows respectively. The scattered light from the sample is collected by the objective and directed to the eye-piece. Figure redrawn from Dmitriev*[109] *and Piller*[110].

6.3 Single particle spectroscopy setup

In order to study single nanoparticles using nanoplasmonic sensing, a single particle spectroscopy setup had to be assembled for this project. The setup had to have several parts, which would serve certain purpose. First of all, there had to be a measurement cell to host the sample with nanostructures and to allow temperature control over the sample as well as contained gaseous environment with controlled flow of gases around the sample. Then the cell had to fit the stage of the optical microscope, which would be used to locate the nanoparticles using dark-field microscopy. Finally, there had to be a spectrometer to be able to measure the scattering signal from the nanostructures. The following is the description of the setup assembled fulfilling all of these conditions.

The measurement cell was purchased from Linkam and it is a temperature-controlled stage THMS600 with working range from -196 to 600°C. The setup is depicted schematically in Figure 19, where one can see the Linkam chamber mounted on the microscope stage (Nikon Eclipse LV100 upright optical microscope). The Linkam stage is connected to a set of mass flow controllers (Bronkhorst) that have several different working ranges to supply the desired flow of reactants to the sample that is put inside the stage in a small quartz cup (see Figure 20). Above the sample cup, the cell has a quartz window, through which it is possible to focus on the nanostructures using the microscope objective, in this case usually a Nikon 50× BD. The sample is then directly illuminated with the microscope's 50 W halogen lamp (Nikon LV-HL50W LL). The scattered light from individual plasmonic nanostructures is collected by an optical fibre (Ocean Optics, UV-vis 200 or 600 μm core), which is connected to the microscope eye-piece tube via a custom made fibre adapter. The collected light is then directed to the entrance slit (500 or 1000 μm) of a spectrometer (Andor Shamrock SR303i) and dispersed using a grating (150 lines/mm, blaze wavelength 800 nm). The scattering spectra are recorded using a thermoelectrically cooled charge-coupled device (CCD) camera (Andor Newton). The setup (particularly, microscope with measurement cell and spectrometer) stands on a floating optical table (Newport), which provides a flat and stable surface and helps to eliminate vibrations from the environment.

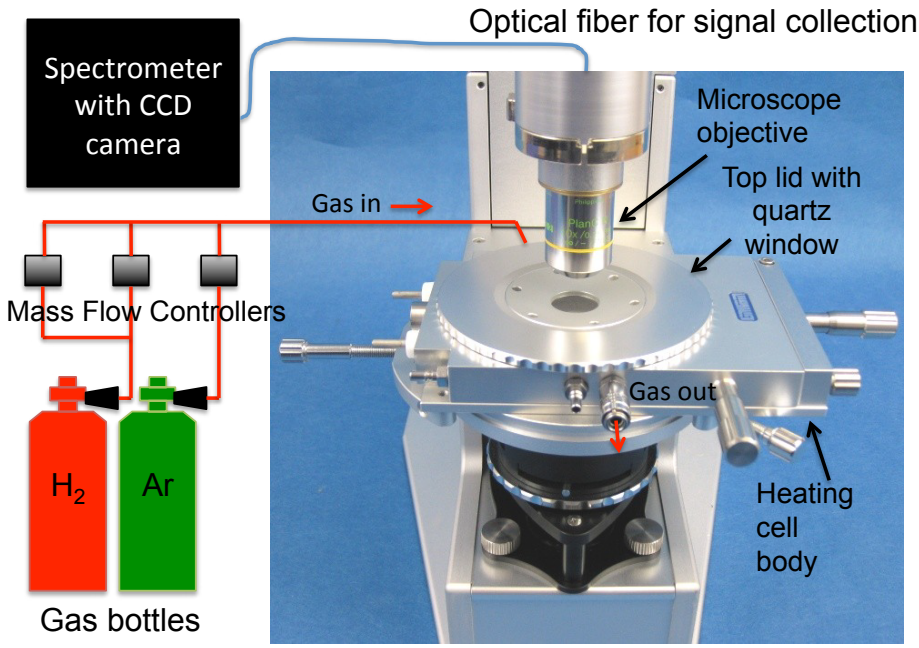

Figure 19. *The schematics of the whole setup: gases are supplied through a range of MFCs to the Linkam chamber located on an optical microscope stage. The chamber has a quartz window, through which one can focus on the sample inside the chamber via a microscope objective. The scattering signal from the nanoparticles dispersed on the sample in focus is collected with an optical fibre that is attached to the microscope eye-piece via a custom made fibre adapter (not shown). The signal is directed through the fibre to the spectrometer with CCD camera.*

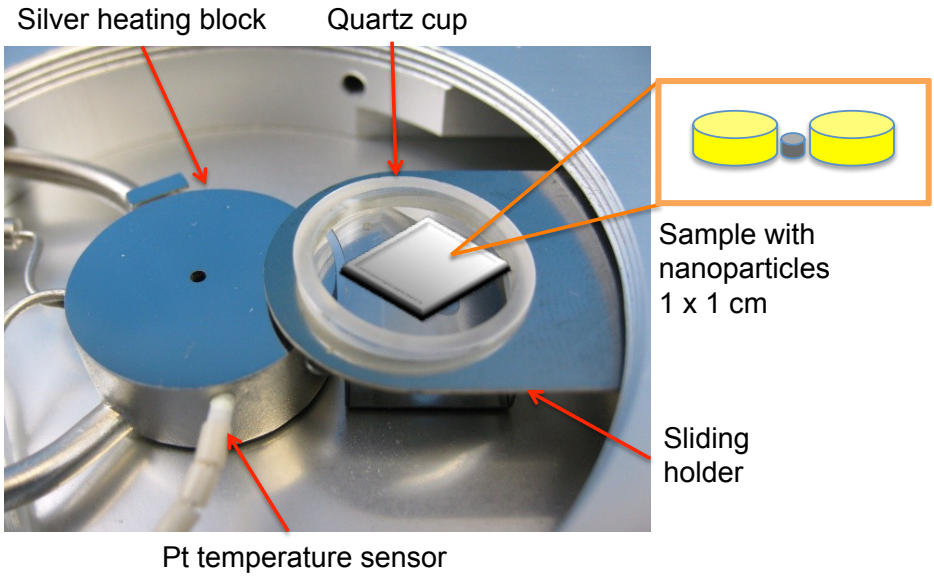

Figure 20. *View of the Linkam chamber with the top lid removed: one can see the Ag heating block and the partly retracted quartz cup containing the sample. The cup with the sample piece is placed exactly above the heating block with the help of a sliding holder. The Pt resistor T-sensor mounted inside the Ag block, accurate to 0.1°C, provides a stable temperature signal and feedback to the temperature controller.*

6.3.1 Signal acquisition

At 50× objective magnification (it is not possible to use a 100× objective, since its working distance is too short for the Linkam chamber), the estimated sampling area with a 600 μm core fibre is about 12.5 μm^2, which allows for selective collection of the scattered light from individual nanoantennas fabricated/dispersed at low density on the sample surface. Normalized scattering spectra with intensity I_{sc} are obtained from individual plasmonic particles as a function of wavelength λ using the relation $I_{sc}(\lambda) = (S(\lambda) - D(\lambda))/CRS(\lambda)$, where $S(\lambda)$ is the collected signal from an area with nanoantenna, $D(\lambda)$ is the signal from the nearby area without nanoantenna (dark signal for background correction), and $CRS(\lambda)$ is the signal collected from a diffuse white certified reflectance standard (Labsphere SRS-99-020). $CRS(\lambda)$ was used in order to correct the signal for the lamp emission spectrum, which is strongly wavelength-dependent. The acquisition time for each spectrum was varied depending on the measurement needs from 0.125 s to 10 s.

7 SUMMARY AND OUTLOOK

The results of this thesis are presented in three appended papers, for which a brief summary is given in this chapter, followed by a short outlook.

7.1 Summary of appended papers

The work presented in **Paper I** was motivated by the fact that, in order to utilize the strong electric field enhancement in the hot spot of plasmonic nanoantennas for sensing in a materials science context, it is crucial to be able to place a nanoobject of interest with high accuracy in such a hot spot. This is problematic with state-of-the-art nanofabrication approaches, especially when several materials are to be used, small gaps are required and large surface areas are to be patterned. In the paper we present a novel fabrication method called Shrinking-Hole Colloidal Lithography (SHCL), which is a further development of the established Hole-mask Colloidal Lithography (HCL) technique. In SHCL we introduce three different variations of a critical step that exploits a "shrinking hole" effect to enhance the versatility of HCL. The effect of the "shrinking hole" arises from the fact that, as material is deposited through the hole-mask created in the HCL process, it also continuously builds up at the rims of the hole, thus causing it to shrink continuously. We show that this effect can be utilized systematically in combination with the growth of sacrificial nanostructures. Depending on the specifics of the targeted application and desired material combinations of the final structure, the sacrificial nanostructure that is grown in order to shrink the hole in the mask to the required size (so that it can be used to grow a smaller nanoparticle) can constitute (i) a C nanocone, (ii) a Cr nanocone or (iii) a Cr funnel. If exploited carefully, as demonstrated in the paper, this approach provides unique possibilities for the self-aligned crafting of complex multimaterial nanostructures with high level of control over the size and position of the constituent elements. As in HCL, the method also preserves the ability of patterning large areas (few cm^2) with aligned complex nanostructures. To illustrate the possibilities, we demonstrate the fabrication of several complex plasmonic nanoantennas, such as: nanodisc dimer with small Pd particle in the hot-spot, cascaded Au trimer, Au-Pd disc heterodimer and Au disc with small Pd and Al_2O_3 particles on each side. In the second part of the paper we show on two specific examples what kind of sensing functionality that can be achieved with the fabricated structures. In the first example, we demonstrate an all-optical self-referenced hydrogen sensor based on light polarization that is comprised of an array of an Au nanodiscs with a smaller adjacent Pd particle. In

the second example, we demonstrate the single particle hydrogen sensing capability of an Au nanodisc dimer with small Pd particle in the dimer gap.

The main focus of **Paper II** is the development of a synthesis strategy for the self-assembly of two different individual colloidal nanoparticles into *hetero*dimers. Utilizing electrostatic interactions, we show the possibilities to combine oppositely charged individual nanoparticles of different sizes, shapes and materials into heterodimer combinations. Using this approach the following heterodimers were obtained: Au or Ag spheres of 90 nm paired with Au cubes (30 nm) or Au rhombic dodecahedra (50 nm), as well as combinations of Pd nanoparticles of different sizes and shapes (cubes of 25 or 70 nm, rhombic dodecahedra of 110 nm, truncated cubes of 120 nm, octahedra of 130 nm) with Au or Ag spheres of 90 nm. We show that the aggregation process can be controlled to produce the highest possible yield of dimers by tuning the ratio between the two different nanoparticle components. The synthesis results are rationalized with the aid of theoretical modelling. Such coupled nanoparticle systems possess new properties and are interesting for numerous applications. As a basic example, we demonstrate the possibility of sensing a catalytic process such as hydrogen dissociation and absorption in a single Pd nanocube by using the Au plasmonic unit as the probe for the reaction that is taking place on the adjacent Pd particle.

In **Paper III**, we make use of the Au-Pd heterodimers synthesized with the method described in **Paper II**, and further utilize the sensing capabilities of the plasmonic Au unit in order to investigate processes happening in/on adjacent Pd nanoparticle at the single particle level. Specifically, we study size and shape effects on the thermodynamic properties of hydrogen absorption in Pd. This is motivated by the fact that it is essential to gain deeper understanding of the role of particle specific features in the metal-hydrogen interactions at the nanoscale, since this can help optimizing the performance of hydride-forming materials, as well as to unearth the physics of phase transitions in shape-selected nanocrystals. Moreover the detailed studies of hydrogen interaction with nanoscale Pd systems (focusing mainly on ensembles of Pd nanoparticles) have began only recently and yield contradicting results as well as provoke interesting questions regarding the details of the process. Single particle studies should help eliminate the issues caused by the inhomogeneous sample effects that potentially blur important details of the role of nanoparticle size, shape and local chemical composition on both hydrogen sorption kinetics and thermodynamics. We investigate the hydrogen absorption in Pd nanocubes with size ranging from 45 to 20 nm and measure phase transition isotherms. We quantify the thermodynamics of the process by analysing changes in enthalpy and entropy of hydrogen absorption for individual cubes. In addition, we investigate other Pd particle shapes, such as octahedron and rod. As a result, we find consistent size- and shape-independent thermodynamics in agreement with classic understanding of the first order phase transition for hydride formation in metals.

7.2 Outlook

There are many possibilities to continue the work presented in this thesis, since it to a large extent dealt with the development of the necessary tools for single particle plasmonic nanospectroscopy for materials science and catalysis applications. With these tools now at hand, the fun part only begins. For example, as continuation of **Paper I**, it would be interesting to test sensing capabilities of other arrangements such as cascaded nanodisc trimers, asymmetric dimers and symmetric trimers as shown in Figure 11f – h. According to theoretical studies[114,115] the field enhancement in these structures should be even higher than the one in a homogeneous dimer arrangement, with the consequence of higher sensitivities. This implies the prospects to be able to investigate even smaller catalytic particles, ideally in the sub 10 nm size range, where strong size-effects are predicted.

Another interesting route is to test various dielectric spacer layers, as shown in Figure 11e, for the protection of the plasmonic antenna structure. This becomes important if the nanoantenna is to be used in harsh experimental conditions, such as high temperatures and aggressive gas environments. Heat treatment causes the Au nanoparticles to recrystallize and change their shape at temperatures starting already at 100°C. At even higher temperatures Au atoms become highly mobile and there is a tendency to reduce the total surface area of the particle, which is energetically more favourable[116]. In case of, for example, Ag nanoparticles, which actually support stronger LSPR (and thus have narrower peaks, which is advantageous for sensing) than Au, adding a spacer layer may help to protect them from oxidation to which Ag is prone even in air. Moreover, no matter the plasmonic material, there is always a risk that high temperatures may cause fusion of the sensor elements with a particle deposited in the gap, which also could be avoided by capping the antenna elements with a dielectric layer. Good candidates for spacer layers are for example SiO_2, Al_2O_3, silicon nitride (Si_3N_4), aluminium nitride (AlN), etc. Thin films of such materials can be made with methods like chemical vapour deposition (CVD), plasma-enhanced CVD (PECVD) and atomic layer deposition (ALD). It is also important to note that the use of dielectric spacer layers can make it possible to investigate the role of catalyst support material in a catalytic reaction, which in many cases is critical for the catalyst activity and selectivity.

With regards to the results of **Paper II** and **III**, it is as well obvious that the plasmonic particle used, i.e. the Au sphere, is not the most advantageous shape for sensing purposes as it features much lower field enhancement compared to nanoparticles with more distinct shapes. Therefore, it will be extremely interesting to try new arrangements, for example, an Au rod, an Au triangle, or any other shape that has pointy edges or sides that feature strong field enhancements, with an interesting particle attached to it. Similarly, as mentioned above for nanofabricated nanoparticles, adding a spacer layer around the plasmonic unit of the synthesized nanoparticles is of high interest. Fortunately, there are possibilities to grow spacer layers around metal nanoparticles with wet chemistry methods, for example, shells of SiO_2[117].

As was mentioned earlier, the nanolithography approaches for nanofabrication are efficient for making ordered arrays of complex nanostructures on surfaces. However, they lack the ability to precisely control the shape, size, crystallinity and also composition (if e.g. alloys are desired) of the particle of interest. Therefore, it would be interesting to combine the fabrication approaches of **Paper I** and **Papers II**, **III**, i.e. nanolithography with wet chemical synthesis. For example, the fabricated dimer or trimer arrangements could have a particle with specific chemistry deposited in their junctions, and then the synthesised particle with well-defined size and shape could be bound to the hot spot. The latter could be possible using a tailored linker molecule (present on the surface of the synthesized particle), which specifically binds to the specific surface chemistry provided in the hot spot only by locally growing, e.g small patches of TiO_2, Al_2O_3, which contrast the surface chemistry of the rest of the support. In such a way, it could be possible to bind not only synthesized particles but also, for example, quantum dots (QD) specifically to the hot spot. The latter are interesting due to their tunable fluorescent properties, as well as the possibility to boost these properties by placing a QD in the region of the high field enhancement, and to investigate phenomena such as strong coupling of two oscillators.

Finally, it will also be important and interesting to try any of the above arrangements in a "real" catalytic process. That could be, for example, formation of water on the surface of Pt or Pd by reacting hydrogen and oxygen, the oxidation of carbon monoxide or the conversion of nitrogen oxides (NO_x) on Pt. These studies should as well be aimed at revealing size/shape effects of the particle in question with respect to the investigated catalytic process.

8 ACKNOWLEDGEMENTS

I would like to say thank you to the best people who helped me along the way to achieve the results that are presented in this thesis:

- Christoph Langhammer, my supervisor, who can always find the right words for inspiring, motivating and supporting me.
- Henrik Grönbeck, my examiner, Igor Zoric, my former supervisor and Anders Hellman, my assistant supervisor.
- Carl Wadell, for the great collaborations, discussions and travels together.
- Kasper Moth-Poulsen and the crew: Yuri Antonio Diaz Fernandez, Tina Gschneidtner and Giammarco Nalin, who are wonderful collaborators and as well can do wonders in a beaker.
- Tomasz Antosiewicz and Dominika Świtlik for our great theory collaboration.
- MC2 cleanroom staff, especially Henrik Frederiksen, who was always there for me to help with nanofabrication.
- Joachim Fritzsche, for productive discussions and chocolate!
- All the members of the Chemical Physics group, which is a very nice group to be part of!
- My family and friends!

9 BIBLIOGRAPHY

1 Glover, R. D., Miller, J. M. & Hutchison, J. E. Generation of Metal Nanoparticles from Silver and Copper Objects: Nanoparticle Dynamics on Surfaces and Potential Sources of Nanoparticles in the Environment. *ACS Nano* **5**, 8950-8957, doi:10.1021/nn2031319 (2011).

2 Barber, D. J. & Freestone, I. C. AN INVESTIGATION OF THE ORIGIN OF THE COLOUR OF THE LYCURGUS CUP BY ANALYTICAL TRANSMISSION ELECTRON MICROSCOPY. *Archaeometry* **32**, 33-45, doi:10.1111/j.1475-4754.1990.tb01079.x (1990).

3 Walter, P., Welcomme, E., Hallégot, P., Zaluzec, N. J., Deeb, C., Castaing, J., Veyssière, P., Bréniaux, R., Lévêque, J.-L. & Tsoucaris, G. Early Use of PbS Nanotechnology for an Ancient Hair Dyeing Formula. *Nano Letters* **6**, 2215-2219, doi:10.1021/nl061493u (2006).

4 Agasti, S. S., Rana, S., Park, M.-H., Kim, C. K., You, C.-C. & Rotello, V. M. Nanoparticles for detection and diagnosis. *Advanced Drug Delivery Reviews* **62**, 316-328, doi:http://dx.doi.org/10.1016/j.addr.2009.11.004 (2010).

5 Haley, B. & Frenkel, E. Nanoparticles for drug delivery in cancer treatment. *Urologic Oncology: Seminars and Original Investigations* **26**, 57-64, doi:http://dx.doi.org/10.1016/j.urolonc.2007.03.015 (2008).

6 Huang, H. S. & Hainfeld, J. F. Intravenous magnetic nanoparticle cancer hyperthermia. *International Journal of Nanomedicine* **8**, 2521-2532, doi:10.2147/ijn.s43770 (2013).

7 Pradeep, T. & Anshup. Noble metal nanoparticles for water purification: A critical review. *Thin Solid Films* **517**, 6441-6478, doi:http://dx.doi.org/10.1016/j.tsf.2009.03.195 (2009).

8 Karn, B., Kuiken, T. & Otto, M. Nanotechnology and in situ remediation: a review of the benefits and potential risks. *Ciencia & Saude Coletiva* **16**, 165-178 (2011).

9 Zang, L. *Energy Efficiency and Renewable Energy Through Nanotechnology*. (Springer, 2011).

10 Bell, A. T. The Impact of Nanoscience on Heterogeneous Catalysis. *Science* **299**, 1688-1691 (2003).

11 Rodriguez, J. A., Hanson, J. C. & Chupas, P. J. *In-situ Characterization of Heterogeneous Catalysts*. (Wiley, 2013).

12 Meier, J., Friedrich, K. A. & Stimming, U. Novel method for the investigation of single nanoparticle reactivity. *Faraday Discussions* **121**, 365-372, doi:10.1039/b200014h (2002).

13 Tel-Vered, R. & Bard, A. J. Generation and Detection of Single Metal Nanoparticles Using Scanning Electrochemical Microscopy Techniques†. *The Journal of Physical Chemistry B* **110**, 25279-25287, doi:10.1021/jp064434d (2006).

14 Xiao, X. & Bard, A. J. Observing Single Nanoparticle Collisions at an Ultramicroelectrode by Electrocatalytic Amplification. *Journal of the American Chemical Society* **129**, 9610-9612, doi:10.1021/ja072344w (2007).

15 Roeffaers, M. B. J., Sels, B. F., Uji-i, H., De Schryver, F. C., Jacobs, P. A., De Vos, D. E. & Hofkens, J. Spatially resolved observation of crystal-face-dependent catalysis by single turnover counting. *Nature* **439**, 572-575, doi:http://www.nature.com/nature/journal/v439/n7076/suppinfo/nature04502_S1.html (2006).

16 van Schrojenstein Lantman, E. M., Deckert-Gaudig, T., Mank, A. J. G., Deckert, V. & Weckhuysen, B. M. Catalytic processes monitored at the nanoscale with tip-enhanced Raman spectroscopy. *Nat Nano* **7**, 583-586, doi:http://www.nature.com/nnano/journal/v7/n9/abs/nnano.2012.131.html#supplementary-information (2012).

17 de Smit, E., Swart, I., Creemer, J. F., Hoveling, G. H., Gilles, M. K., Tyliszczak, T., Kooyman, P. J., Zandbergen, H. W., Morin, C., Weckhuysen, B. M. & de Groot, F. M. F. Nanoscale chemical imaging of a working catalyst by scanning transmission X-ray microscopy. *Nature* **456**, 222-225 (2008).

18 Langhammer, C., Zorić, I., Kasemo, B. & Clemens, B. M. Hydrogen Storage in Pd Nanodisks Characterized with a Novel Nanoplasmonic Sensing Scheme. *Nano Letters* **7**, 3122-3127, doi:10.1021/nl071664a (2007).

19 Langhammer, C., Larsson, E. M., Kasemo, B. & Zorić, I. Indirect Nanoplasmonic Sensing: Ultrasensitive Experimental Platform for Nanomaterials Science and Optical Nanocalorimetry. *Nano Letters* **10**, 3529-3538, doi:10.1021/nl101727b (2010).

20 Li, K., Qin, W., Xu, Y., Peng, T. & Li, D. Optical approaches in study of nanocatalysis with single-molecule and single-particle resolution. *Frontiers of Optoelectronics*, 1-15, doi:10.1007/s12200-014-0423-5 (2014).

21 Sambur, J. B. & Chen, P. Approaches to Single-Nanoparticle Catalysis. *Annual Review of Physical Chemistry* **65**, 395-422, doi:10.1146/annurev-physchem-040513-103729 (2014).

22 Hansen, P. L., Wagner, J. B., Helveg, S., Rostrup-Nielsen, J. R., Clausen, B. S. & Topsøe, H. Atom-Resolved Imaging of Dynamic Shape Changes in Supported Copper Nanocrystals. *Science* **295**, 2053-2055 (2002).

23 Boyes, E. D., Ward, M. R., Lari, L. & Gai, P. L. ESTEM imaging of single atoms under controlled temperature and gas environment conditions in catalyst reaction studies. *Annalen der Physik* **525**, 423-429, doi:10.1002/andp.201300068 (2013).

24 Vendelbo, S. B., Elkjær, C. F., Falsig, H., Puspitasari, I., Dona, P., Mele, L., Morana, B., Nelissen, B. J., van Rijn, R., Creemer, J. F., Kooyman, P. J. & Helveg, S. Visualization of oscillatory behaviour of Pt nanoparticles catalysing CO oxidation. *Nat Mater* **13**, 884-890, doi:10.1038/nmat4033

http://www.nature.com/nmat/journal/v13/n9/abs/nmat4033.html - supplementary-information (2014).

25 Creemer, J. F., Helveg, S., Hoveling, G. H., Ullmann, S., Molenbroek, A. M., Sarro, P. M. & Zandbergen, H. W. Atomic-scale electron microscopy at ambient pressure. *Ultramicroscopy* **108**, 993-998, doi:http://dx.doi.org/10.1016/j.ultramic.2008.04.014 (2008).

26 Li, G., Kobayashi, H., Taylor, J. M., Ikeda, R., Kubota, Y., Kato, K., Takata, M., Yamamoto, T., Toh, S., Matsumura, S. & Kitagawa, H. Hydrogen storage in Pd nanocrystals covered with a metal–organic framework. *Nat Mater* **13**, 802-806, doi:10.1038/nmat4030

http://www.nature.com/nmat/journal/v13/n8/abs/nmat4030.html - supplementary-information (2014).

27 Baldi, A., Narayan, T. C., Koh, A. L. & Dionne, J. A. In situ detection of hydrogen-induced phase transitions in individual palladium nanocrystals. *Nat Mater* **advance online publication**, doi:10.1038/nmat4086

http://www.nature.com/nmat/journal/vaop/ncurrent/abs/nmat4086.html - supplementary-information (2014).

28 Langhammer, C. & Larsson, E. M. Nanoplasmonic In Situ Spectroscopy for Catalysis Applications. *ACS Catalysis* **2**, 2036-2045, doi:10.1021/cs300423a (2012).

29 Mie, G. Beiträge zur Optik trüber Medien, speziell kolloidaler Metallösungen. *Annalen der Physik* **330**, 377-445, doi:10.1002/andp.19083300302 (1908).

30 Bohren, C. F. & Huffman, D. R. *Absorption and scattering of light by small particles*. (Wiley, 1983).

31 Mirkin, C. A. & Niemeyer, C. M. *Nanobiotechnology II: More Concepts and Applications*. (John Wiley & Sons, 2007).

32 Mishchenko, M. I., Hovenier, J. W. & Travis, L. D. *Light Scattering by Nonspherical Particles: Theory, Measurements, and Applications*. (Academic Press, 2000).

33 Jain, P. K., Lee, K. S., El-Sayed, I. H. & El-Sayed, M. A. Calculated Absorption and Scattering Properties of Gold Nanoparticles of Different Size, Shape, and Composition: Applications in Biological Imaging and Biomedicine. *The Journal of Physical Chemistry B* **110**, 7238-7248, doi:10.1021/jp057170o (2006).

34 Hao, E. & Schatz, G. C. Electromagnetic fields around silver nanoparticles and dimers. *Journal of Chemical Physics* **120**, 357-366, doi:10.1063/1.1629280 (2004).

35 Hao, F., Nehl, C. L., Hafner, J. H. & Nordlander, P. Plasmon Resonances of a Gold Nanostar. *Nano Letters* **7**, 729-732, doi:10.1021/nl062969c (2007).

36 Wang, H., Brandl, D. W., Le, F., Nordlander, P. & Halas, N. J. Nanorice: A Hybrid Plasmonic Nanostructure. *Nano Letters* **6**, 827-832, doi:10.1021/nl060209w (2006).

37 Wu, Y. & Nordlander, P. Plasmon hybridization in nanoshells with a nonconcentric core. *The Journal of Chemical Physics* **125**, -, doi:doi:http://dx.doi.org/10.1063/1.2352750 (2006).

38 Knight, M. W. & Halas, N. J. Nanoshells to nanoeggs to nanocups: optical properties of reduced symmetry core–shell nanoparticles beyond the quasistatic limit. *New Journal of Physics* **10**, 105006 (2008).

39 Wokaun, A., Gordon, J. P. & Liao, P. F. Radiation Damping in Surface-Enhanced Raman Scattering. *Physical Review Letters* **48**, 957-960 (1982).

40 Shalaev, V. M. & Kawata, S. *Nanophotonics with Surface Plasmons*. (Elsevier, 2007).

41 Langhammer, C., Yuan, Z., Zorić, I. & Kasemo, B. Plasmonic Properties of Supported Pt and Pd Nanostructures. *Nano Letters* **6**, 833-838, doi:10.1021/nl060219x (2006).

42 Kittel, C. *Introduction to solid state physics*. (1956).

43 Kanehara, M., Koike, H., Yoshinaga, T. & Teranishi, T. Indium Tin Oxide Nanoparticles with Compositionally Tunable Surface Plasmon Resonance Frequencies in the Near-IR Region. *Journal of the American Chemical Society* **131**, 17736-17737, doi:10.1021/ja9064415 (2009).

44 Zhao, Y., Pan, H., Lou, Y., Qiu, X., Zhu, J., Burda, C. Plasmonic Cu2−xS Nanocrystals: Optical and Structural Properties of Copper-Deficient Copper(I) Sulfides. *Journal of the American Chemical Society* **131**, 4253-4261, doi:10.1021/ja805655b (2009).

45 Dorfs, D., Härtling, T., Miszta, K., Bigall, N. C., Kim, M. R., Genovese, A., Falqui, A., Povia, M. & Manna, L. Reversible Tunability of the Near-Infrared Valence Band Plasmon Resonance in Cu2–xSe Nanocrystals. *Journal of the American Chemical Society* **133**, 11175-11180, doi:10.1021/ja2016284 (2011).

46 Grigorenko, A. N., Polini, M. & Novoselov, K. S. Graphene plasmonics. *Nat Photon* **6**, 749-758 (2012).

47 Tassin, P., Koschny, T., Kafesaki, M. & Soukoulis, C. M. A comparison of graphene, superconductors and metals as conductors for metamaterials and plasmonics. *Nat Photon* **6**, 259-264, doi:http://www.nature.com/nphoton/journal/v6/n4/abs/nphoton.2012.27.html - supplementary-information (2012).

48 Ma, X., Dai, Y., Yu, L. & Huang, B. Noble-metal-free plasmonic photocatalyst: hydrogen doped semiconductors. *Sci. Rep.* **4**, doi:10.1038/srep03986 (2014).

49 Geim, A. K. & Novoselov, K. S. The rise of graphene. *Nat Mater* **6**, 183-191 (2007).

50 Bonaccorso, F., Sun, Z., Hasan, T. & Ferrari, A. C. Graphene photonics and optoelectronics. *Nat Photon* **4**, 611-622 (2010).

51 Michaels, A. M., Jiang & Brus, L. Ag Nanocrystal Junctions as the Site for Surface-Enhanced Raman Scattering of Single Rhodamine 6G Molecules. *The Journal of Physical Chemistry B* **104**, 11965-11971, doi:10.1021/jp0025476 (2000).

52 Rechberger, W., Hohenau, A., Leitner, A., Krenn, J. R., Lamprecht, B. & Aussenegg, F. R. Optical properties of two interacting gold nanoparticles. *Optics Communications* **220**, 137-141, doi:10.1016/s0030-4018(03)01357-9 (2003).

53 Gunnarsson, L., Rindzevicius, T., Prikulis, J., Kasemo, B., Käll, M., Zou, S. & Schatz, G. C. Confined Plasmons in Nanofabricated Single Silver Particle Pairs: Experimental Observations of Strong Interparticle Interactions. *The Journal of Physical Chemistry B* **109**, 1079-1087, doi:10.1021/jp049084e (2004).

54 Song, J.-H., Hong, S.-Y., Kim, Y.-G., Lee, K.-W. & Kim, Y.-Y. Observation of plasmon hybridization in gold nanoparticle pairs. *Journal of the Korean Physical Society* **50**, 558-562 (2007).

55 Jain, P. K. & El-Sayed, M. A. Surface plasmon coupling and its universal size scaling in metal nanostructures of complex geometry: Elongated particle pairs and nanosphere trimers. *Journal of Physical Chemistry C* **112**, 4954-4960, doi:10.1021/jp7120356 (2008).

56 Jain, P. K. & El-Sayed, M. A. Noble Metal Nanoparticle Pairs: Effect of Medium for Enhanced Nanosensing. *Nano Letters* **8**, 4347-4352, doi:10.1021/nl8021835 (2008).

57 Acimovic, S. S., Kreuzer, M. P., Gonzalez, M. U. & Quidant, R. Plasmon Near-Field Coupling in Metal Dimers as a Step toward Single-Molecule Sensing. *ACS Nano* **3**, 1231-1237, doi:10.1021/nn900102j (2009).

58 Dadosh, T., Sperling, J., Bryant, G. W., Breslow, R., Shegai, T., Dyshel, M., Haran, G. & Bar-Joseph, I. Plasmonic Control of the Shape of the Raman Spectrum of a Single Molecule in a Silver Nanoparticle Dimer. *ACS Nano* **3**, 1988-1994, doi:10.1021/nn900422w (2009).

59 Cheng, Y., Wang, M., Borghs, G. & Chen, H. Gold Nanoparticle Dimers for Plasmon Sensing. *Langmuir* **27**, 7884-7891, doi:10.1021/la200840m (2011).

60 Halas, N. J., Lal, S., Chang, W.-S., Link, S. & Nordlander, P. Plasmons in Strongly Coupled Metallic Nanostructures. *Chemical Reviews* **111**, 3913-3961, doi:10.1021/cr200061k (2011).

61 Tittl, A., Kremers, C., Dorfmueller, J., Chigrin, D. N. & Giessen, H. Spectral shifts in optical nanoantenna-enhanced hydrogen sensors. *Optical Materials Express* **2**, 111-118 (2012).

62 Jain, P. K. & El-Sayed, M. A. Universal Scaling of Plasmon Coupling in Metal Nanostructures: Extension from Particle Pairs to Nanoshells. *Nano Letters* **7**, 2854-2858, doi:10.1021/nl071496m (2007).

63 Jain, P. K., Huang, W. & El-Sayed, M. A. On the Universal Scaling Behavior of the Distance Decay of Plasmon Coupling in Metal Nanoparticle Pairs: A Plasmon Ruler Equation. *Nano Letters* **7**, 2080-2088, doi:10.1021/nl071008a (2007).

64 Lassiter, J. B., Aizpurua, J., Hernandez, L. I., Brandl, D. W., Romero, I., Lal, S., Hafner, J. H., Nordlander, P. & Halas, N. J. Close Encounters between Two Nanoshells. *Nano Letters* **8**, 1212-1218, doi:10.1021/nl080271o (2008).

65 Boyer, D., Tamarat, P., Maali, A., Lounis, B. & Orrit, M. Photothermal Imaging of Nanometer-Sized Metal Particles Among Scatterers. *Science* **297**, 1160-1163 (2002).

66 Billaud, P., Marhaba, S., Grillet, N., Cottancin, E., Bonnet, C., Lermé, J., Vialle, J.-L., Broyer, M. & Pellarin, M. Absolute optical extinction measurements of single nano-objects by spatial modulation spectroscopy using a white lamp. *Review of Scientific Instruments* **81**, -, doi:doi:http://dx.doi.org/10.1063/1.3340875 (2010).

67 Kumar, C. S. S. R. *Raman Spectroscopy for Nanomaterials Characterization*. (Springer, 2012).

68 Shen, Y. R. Surface properties probed by second-harmonic and sum-frequency generation. *Nature* **337**, 519-525 (1989).

69 Ohtsu, M. *Progress in Nanophotonics 1*. (Springer, 2011).

70 Douillard, L., Charra, F., Fiorini, C., Adam, P. M., Bachelot, R., Kostcheev, S., Lerondel, G., Lamy de la Chapelle, M. & Royer, P. Optical properties of metal nanoparticles as probed by photoemission electron microscopy. *Journal of Applied Physics* **101**, -, doi:doi:http://dx.doi.org/10.1063/1.2719282 (2007).

71 Grubisic, A., Ringe, E., Cobley, C. M., Xia, Y., Marks, L. D., Van Duyne, R. P. & Nesbitt, D. J. Plasmonic Near-Electric Field Enhancement Effects in Ultrafast Photoelectron Emission: Correlated Spatial and Laser Polarization Microscopy Studies of Individual Ag Nanocubes. *Nano Letters* **12**, 4823-4829, doi:10.1021/nl302271u (2012).

72 Chaturvedi, P., Hsu, K. H., Kumar, A., Fung, K. H., Mabon, J. C. & Fang, N. X. Imaging of Plasmonic Modes of Silver Nanoparticles Using High-Resolution Cathodoluminescence Spectroscopy. *ACS Nano* **3**, 2965-2974, doi:10.1021/nn900571z (2009).

73 García de Abajo, F. J. & Kociak, M. Probing the Photonic Local Density of States with Electron Energy Loss Spectroscopy. *Physical Review Letters* **100**, 106804 (2008).

74 Ringe, E., Sharma, B., Henry, A.-I., Marks, L. D. & Van Duyne, R. P. Single nanoparticle plasmonics. *Physical Chemistry Chemical Physics* **15**, 4110-4129, doi:10.1039/c3cp44574g (2013).

75 Liu, N., Tang, M. L., Hentschel, M., Giessen, H. & Alivisatos, A. P. Nanoantenna-enhanced gas sensing in a single tailored nanofocus. *Nature Materials* **10**, 631-636, doi:10.1038/nmat3029 (2011).

76 Shegai, T. & Langhammer, C. Hydride Formation in Single Palladium and Magnesium Nanoparticles Studied By Nanoplasmonic Dark-Field Scattering Spectroscopy. *Advanced Materials* **23**, 4409-+, doi:10.1002/adma.201101976 (2011).

77 Fukai, Y. *The Metal-Hydrogen System*. (Springer-Verlag, 1993).

78 Schlapbach, L., SpringerLink, A. & SpringerLink. *Hydrogen in Intermetallic Compounds I: Electronic, Thermodynamic, and Crystallographic Properties, Preparation*. Vol. 63 (Springer-Verlag, 1988).

79 Schwarz, R. B. & Khachaturyan, A. G. Thermodynamics of open two-phase systems with coherent interfaces: Application to metal–hydrogen systems. *Acta Materialia* **54**, 313-323, doi:http://dx.doi.org/10.1016/j.actamat.2005.08.044 (2006).

80 Hughes, R. C., Schubert, W. K., Zipperian, T. E., Rodriguez, J. L. & Plut, T. A. Thin-film palladium and silver alloys and layers for metal-insulator-semiconductor sensors. *Journal of Applied Physics* **62**, 1074-1083, doi:doi:http://dx.doi.org/10.1063/1.339738 (1987).

81 Hughes, R. C. & Schubert, W. K. Thin films of Pd/Ni alloys for detection of high hydrogen concentrations. *Journal of Applied Physics* **71**, 542-544, doi:doi:http://dx.doi.org/10.1063/1.350646 (1992).

82 Westerwaal, R. J., Rooijmans, J. S. A., Leclercq, L., Gheorghe, D. G., Radeva, T., Mooij, L., Mak, T., Polak, L., Slaman, M., Dam, B. & Rasing, T. Nanostructured Pd–Au based fiber optic sensors for probing hydrogen concentrations in gas mixtures. *International Journal of Hydrogen Energy* **38**, 4201-4212, doi:http://dx.doi.org/10.1016/j.ijhydene.2012.12.146 (2013).

83 Graham, T. On the Absorption and Dialytic Separation of Gases by Colloid Septa. *Philosophical Transactions of the Royal Society of London* **156**, 399-439, doi:10.2307/108953 (1866).

84 Niu, W., Zhang, L. & Xu, G. Shape-Controlled Synthesis of Single-Crystalline Palladium Nanocrystals. *ACS Nano* **4**, 1987-1996, doi:10.1021/nn100093y (2010).

85 Bardhan, R., Hedges, L. O., Pint, C. L., Javey, A., Whitelam, S. & Urban, J. J. Uncovering the intrinsic size dependence of hydriding phase transformations in nanocrystals. *Nat Mater* **12**, 905-912, doi:10.1038/nmat3716

http://www.nature.com/nmat/journal/v12/n10/abs/nmat3716.html -supplementary-information (2013).

86 Larche, F. C. in *Advances in Phase Transitions* (eds J.D. Embury & G.R. Purdy) p. 193 (Pergamon, 1988).

87 Bérubé, V., Radtke, G., Dresselhaus, M. & Chen, G. Size effects on the hydrogen storage properties of nanostructured metal hydrides: A review. *International Journal of Energy Research* **31**, 637-663, doi:10.1002/er.1284 (2007).

88 Pundt, A., Sachs, C., Winter, M., Reetz, M. T., Fritsch, D. & Kirchheim, R. Hydrogen sorption in elastically soft stabilized Pd-clusters. *Journal of Alloys and Compounds* **293–295**, 480-483, doi:http://dx.doi.org/10.1016/S0925-8388(99)00469-7 (1999).

89 Sachs, C., Pundt, A., Kirchheim, R., Winter, M., Reetz, M. T. & Fritsch, D. Solubility of hydrogen in single-sized palladium clusters. *Physical Review B* **64**, 075408 (2001).

90 Pundt, A., Suleiman, M., Bähtz, C., Reetz, M. T., Kirchheim, R. & Jisrawi, N. M. Hydrogen and Pd-clusters. *Materials Science and Engineering: B* **108**, 19-23, doi:http://dx.doi.org/10.1016/j.mseb.2003.10.029 (2004).

91 Langhammer, C., Zhdanov, V. P., Zorić, I. & Kasemo, B. Size-dependent hysteresis in the formation and decomposition of hydride in metal nanoparticles. *Chem. Phys. Lett.* **488**, 62-66, doi:10.1016/j.cplett.2010.01.071 (2010).

92 Langhammer, C., Zhdanov, V. P., Zorić, I. & Kasemo, B. Size-Dependent Kinetics of Hydriding and Dehydriding of Pd Nanoparticles. *Physical Review Letters* **104**, 135502 (2010).

93 Cui, Z. *Nanofabrication: Principles, Capabilities and Limits*. (Springer, 2008).

94 Zhirnov, V. V. & Herr, D. J. C. New frontiers: self-assembly and nanoelectronics. *Computer* **34**, 34-43, doi:10.1109/2.895116 (2001).

95 Heiz, U. & Landman, U. *Nanocatalysis*. (Springer, 2007).

96 Chi, L. *Nanotechnology: Volume 8: Nanostructured Surfaces*. (John Wiley & Sons, 2010).

97 Fredriksson, H., Alaverdyan, Y., Dmitriev, A., Langhammer, C., Sutherland, D. S., Zaech, M. & Kasemo, B. Hole-mask colloidal lithography. *Advanced Materials* **19**, 4297-4302, doi:10.1002/adma.200700680 (2007).

98 Fredriksson, H. *Nanostructures of Graphite and Amorphous Carbon - Fabrication and Properties* Thesis for the degree of doctor of philosophy thesis, Chalmers University of Technology, (2009).

99 Kreibig, U., Bönnemann, H. & Hormes, J. in *Handbook of Surfaces and Interfaces of Materials* (ed Hari Singh Nalwa) 1-85 (Academic Press, 2001).

100 Siani, A. & Carolina, U. o. S. *Synthesis of Supported Nanoparticles for Catalytic Applications*. (University of South Carolina, 2007).

101 Wu, H.-L., Kuo, C.-H. & Huang, M. H. Seed-Mediated Synthesis of Gold Nanocrystals with Systematic Shape Evolution from Cubic to Trisoctahedral and Rhombic Dodecahedral Structures. *Langmuir* **26**, 12307-12313, doi:10.1021/la1015065 (2010).

102 Niu, W., Li, Z.-Y., Shi, L., Liu, X., Li, H., Han, S., Chen, J. & Xu, G. Seed-Mediated Growth of Nearly Monodisperse Palladium Nanocubes with Controllable Sizes. *Crystal Growth & Design* **8**, 4440-4444, doi:10.1021/cg8002433 (2008).

103 Franssila, S. *Introduction to Microfabrication*. (Wiley, 2004).

104 Dupas, C., Houdy, P. & Lahmani, M. *Nanoscience: Nanotechnologies and Nanophysics*. (Springer, 2007).

105 Rossnagel, S. M., Cuomo, J. J. & Westwood, W. D. *Handbook of Plasma Processing Technology: Fundamentals, Etching, Deposition, and Surface Interactions*. (Noyes Publications, 1990).

106 Mattox, D. M. *Handbook of Physical Vapor Deposition (PVD) Processing*. (Elsevier, 2007).

107 SreeHarsha, K. S. *Principles of physical vapor deposition of thin films*. (Elsevier, 2006).

108 Goldstein, J. *Scanning Electron Microscopy and X-Ray Microanalysis*. (Kluwer Academic/Plenum Publishers, 2003).

109 Dmitriev, A. *Nanoplasmonic Sensors*. (Springer, 2012).

110 Piller, H. *Microscope Photometry*. (Springer London, Limited, 2011).

111 Bacsa, W. S., Pavlenko, E. & Tishkova, V. Optical Interference Substrates for Nanoparticles and Two-Dimensional Materials. *Nanomaterials and Nanotechnology* **3** (2013).

112 Shoute, L. C. T. Multilayer Substrate-Mediated Tuning Resonance of Plasmon and SERS EF of Nanostructured Silver. *Chemphyschem* **11**, 2539-2545, doi:10.1002/cphc.201000351 (2010).

113 Blake, P., Hill, E. W., Castro Neto, A. H., Novoselov, K. S., Jiang, D., Yang, R., Booth, T. J. & Geim, A. K. Making graphene visible. *Applied Physics Letters* **91**, -, doi:doi:http://dx.doi.org/10.1063/1.2768624 (2007).

114 Li, K., Stockman, M. I. & Bergman, D. J. Self-Similar Chain of Metal Nanospheres as an Efficient Nanolens. *Physical Review Letters* **91**, 227402 (2003).

115 Thomas, R. & Swathi, R. S. Organization of Metal Nanoparticles for Surface-Enhanced Spectroscopy: A Difference in Size Matters. *The Journal of Physical Chemistry C* **116**, 21982-21991, doi:10.1021/jp3086914 (2012).

116 Chen, Y., Milenkovic, S. & Hassel, A. W. Thermal stability of {100} facet terminated gold nanobelts. *Applied Surface Science* **258**, 6224-6231, doi:10.1016/j.apsusc.2012.02.144 (2012).

117 Liz-Marzán, L. M., Giersig, M. & Mulvaney, P. Synthesis of Nanosized Gold−Silica Core−Shell Particles. *Langmuir* **12**, 4329-4335, doi:10.1021/la9601871 (1996).

Paper I

Shrinking-Hole Colloidal Lithography: Self-Aligned Nanofabrication of Complex Plasmonic Nanoantennas

Svetlana Syrenova, Carl Wadell and Christoph Langhammer

Nano Letters **14**, 2655-2663, doi:10.1021/nl500514y (2014)

Paper II

A Versatile Self-Assembly Strategy for the Synthesis of Shape-Selected Colloidal Noble Metal Nanoparticle Heterodimers

Tina A. Gschneidtner, Yuri A. Diaz Fernandez, Svetlana Syrenova, Fredrik Westerlund, Christoph Langhammer and Kasper Moth-Poulsen

Langmuir **30**, 3041-3050, doi:10.1021/la5002754 (2014)

Paper III

Indirect Plasmonic Nanospectroscopy of the Hydride Formation Thermodynamics in Individual Shape-Selected Pd Nanocrystals with Different Size

Svetlana Syrenova, Tina A. Gschneidtner, Yuri A. Diaz Fernandez, Giammarco Nalin, Dominika Świtlik, Fredrik Westerlund, Tomasz J. Antosiewicz, Kasper Moth-Poulsen and Christoph Langhammer

In manuscript